

University of Kentucky

UKnowledge

Theses and Dissertations--Earth and
Environmental Sciences

Earth and Environmental Sciences


2022

**DEFORMATION OF WALL ROCKS AND OVERBURDEN SEQUENCES
PROXIMAL TO SALT DIAPIRS IN SALT VALLEY, UTAH:
IMPLICATIONS FOR PREDICTING SUBSEISMIC DAMAGE IN SALT
TECTONIC SYSTEMS**

William Swanger

University of Kentucky, williamswanger@hotmail.com

Author ORCID Identifier:

 <https://orcid.org/0000-0003-3269-0424>

Digital Object Identifier: <https://doi.org/10.13023/etd.2022.169>

[Right click to open a feedback form in a new tab to let us know how this document benefits you.](#)

Recommended Citation

Swanger, William, "DEFORMATION OF WALL ROCKS AND OVERBURDEN SEQUENCES PROXIMAL TO SALT DIAPIRS IN SALT VALLEY, UTAH: IMPLICATIONS FOR PREDICTING SUBSEISMIC DAMAGE IN SALT TECTONIC SYSTEMS" (2022). *Theses and Dissertations--Earth and Environmental Sciences*. 91. https://uknowledge.uky.edu/ees_etds/91

This Master's Thesis is brought to you for free and open access by the Earth and Environmental Sciences at UKnowledge. It has been accepted for inclusion in Theses and Dissertations--Earth and Environmental Sciences by an authorized administrator of UKnowledge. For more information, please contact UKnowledge@lsv.uky.edu.

STUDENT AGREEMENT:

I represent that my thesis or dissertation and abstract are my original work. Proper attribution has been given to all outside sources. I understand that I am solely responsible for obtaining any needed copyright permissions. I have obtained needed written permission statement(s) from the owner(s) of each third-party copyrighted matter to be included in my work, allowing electronic distribution (if such use is not permitted by the fair use doctrine) which will be submitted to UKnowledge as Additional File.

I hereby grant to The University of Kentucky and its agents the irrevocable, non-exclusive, and royalty-free license to archive and make accessible my work in whole or in part in all forms of media, now or hereafter known. I agree that the document mentioned above may be made available immediately for worldwide access unless an embargo applies.

I retain all other ownership rights to the copyright of my work. I also retain the right to use in future works (such as articles or books) all or part of my work. I understand that I am free to register the copyright to my work.

REVIEW, APPROVAL AND ACCEPTANCE

The document mentioned above has been reviewed and accepted by the student's advisor, on behalf of the advisory committee, and by the Director of Graduate Studies (DGS), on behalf of the program; we verify that this is the final, approved version of the student's thesis including all changes required by the advisory committee. The undersigned agree to abide by the statements above.

William Swanger, Student

Dr. J. Ryan Thigpen, Major Professor

Dr. Michael M. McGlue, Director of Graduate Studies

DEFORMATION OF WALL ROCKS AND OVERBURDEN SEQUENCES
PROXIMAL TO SALT DIAPIRS IN SALT VALLEY, UTAH: IMPLICATIONS FOR
PREDICTING SUBSEISMIC DAMAGE IN SALT TECTONIC SYSTEMS

THESIS

A thesis submitted in partial fulfillment of the
requirements for the degree of Master of Science in the
College of Arts & Sciences
at the University of Kentucky

By

William R. Swanger II

Lexington, Kentucky

Director: Dr. J. Ryan Thigpen, Associate Professor of Geology

Lexington, Kentucky

2022

Copyright © William R. Swanger 2022
<https://orcid.org/0000-0003-3269-0424>

ABSTRACT OF THESIS

DEFORMATION OF WALL ROCKS AND OVERBURDEN SEQUENCES PROXIMAL TO SALT DIAPIRS IN SALT VALLEY, UTAH: IMPLICATIONS FOR PREDICTING SUBSEISMIC DAMAGE IN SALT TECTONIC SYSTEMS

Although deformation related to salt tectonics is generally considered to be an ancillary field of structural geology, owing to its relatively limited occurrence in the geologic record, the preponderance of salt-involved systems in multiple hydrocarbon-rich basins around the world (e.g., Gulf of Mexico, Atlantic passive margins, Iran, etc.) creates a necessity for understanding salt-related deformation. Traditionally, salt was considered to be relatively weak and thus was mostly unable to drive deformation of adjacent wall rocks and cover sequences. However, a number of recent numerical modeling studies have shown that mobilized and pressurized salt may have the ability to actively pierce overburden sequences (active diapirism) and drive pervasive deformation. Field evidence of these “damage” zones has remained elusive, but if these active diapirs are the dominant mechanism of salt evolution in many contractional systems, field observations must confirm this. The Salt Valley, Utah, which is a salt-cored breached anticlinal valley, is a perfect natural laboratory to examine deformation and strain accommodation in high porosity sandstones proximal to mobile salt. In Salt Valley, the paleo-salt wall contacts and adjacent sedimentary wall rocks are now exposed at the surface. Deformation in these types of systems is often the result of compaction (pore-collapse) and deformation band localization in high-porosity wall rock and cover sequences proximal to salt diapirs. Mapping transects normal to the paleo-salt wall reveal the presence of steeply dipping (60-75°) normal sense deformation/shear bands that define two plastic strain gradients; a long wavelength strain gradient with deformation band accumulated thicknesses related either to distance from the paleo-salt wall or the valley anticlinal axis, and a short wavelength strain gradient with band accumulations that increase in intensity approaching brittle normal fault planes. Additionally, intense zones of compactional deformation banding are recognized immediately adjacent to the paleo-salt wall (within 10s of m) and in “roof-pendants” in the valley. SEM analysis of deformation band damage zones reveal that the deformation bands preserved in all 26 samples occurred prior to significant cementation, which is here interpreted to indicate that these “rocks” actually behaved as critical-state materials during deformation. In this framework, we interpret that the long wavelength plastic strain gradients likely formed during outer-arc extension and doming of the regional anticlinal fold. The shorter wavelength gradients that increase approaching brittle normal faults, are interpreted to result from increasing extensional plastic strain localization that acts to strain-harden the material, eventually allowing it to fail as a Mohr-Coulomb rock and produce normal

faults. Finally, the compactional plastic strain zones immediately adjacent to salt are interpreted to result from “tunneling” of the salt during active diapirism. These findings increase our understanding of the mechanisms that drive salt-related deformation in high-porosity rocks, and may allow us to better predict subseismic deformation in petroleum systems at depth.

KEYWORDS: Deformation bands, salt diapirs, numerical models, paleo-salt wall, Moab member sandstone, Salt Valley Utah

William Ray Swanger II

1/13/2022

Date

DEFORMATION OF WALL ROCKS AND OVERBURDEN SEQUENCES
PROXIMAL TO SALT DIAPIRS IN SALT VALLEY, UTAH: IMPLICATIONS
FOR PREDICTING SUBSEISMIC DAMAGE IN SALT TECTONIC SYSTEMS

By
William R. Swanger II

Dr. J. Ryan Thigpen

Director of Thesis

Dr. Michael M. McGlue

Director of Graduate Studies

1/13/2022

Date

ACKNOWLEDGMENTS

The following thesis benefited from the insights and direction from several people. First, my thesis advisor, Dr. J. Ryan Thigpen, who pushed our understanding of salt-related deformation structures in the Paradox Basin further than I could have imagined. He also provided exceptional editorial comments that greatly improved the following thesis. Next, I wish to thank my thesis committee members, Dr. William Haneberg and Dr. David Moecher for their guidance. Dr. Moecher also provided valuable training on scanning electron microscope operation and sample analysis that greatly improved my understanding of deformation band structures.

In addition to the technical assistance above, I received equally important assistance from my family and friends. This includes my colleagues in the Structure and Geodynamics Research Group at UK, who provided exceptional intellectual guidance and personal support during our time together. Lastly, my fiancé Trista was a constant source of strength and support during my time at the University of Kentucky, and the following work would not have been possible without her love and patience.

TABLE OF CONTENTS

ACKNOWLEDGMENTS	iii
LIST OF FIGURES	v
1. INTRODUCTION	1
2. BACKGROUND	5
2.1 Evaporite structural systems	5
2.2 Strain accommodation and pervasive plastic “damage” in evaporite systems	8
2.3 Geologic setting of the Paradox Basin study area	12
2.4 Deformation band formation in the Salt Valley.....	13
3. METHODS	13
4. RESULTS	17
4.1 Mesoscale structural transects.....	17
4.2 Petrographic and SEM analyses.....	29
5. DISSCUSSION	34
5.1 Structural petrology of deformation band damage zones in Salt Valley	34
5.2 Plastic strain gradients near fault planes and salt walls	35
5.3 Comparison of results with numerical models of diapir formation	38
6. CONCLUSIONS.....	50
REFERENCES	52
VITA.....	57

LIST OF FIGURES

Figure 1. Regional map of the Paradox Basin	3
Figure 2. Geologic map of the northeastern portion of the Paradox Basin.....	4
Figure 3. Schematic diagram of a gravity-driven deformation system.....	5
Figure 4. Schematic cross sections of different diapir styles.....	6
Figure 5. Mohr-Coulomb and critical state failure criteria	10
Figure 6. Deformation bands create in the lab.....	11
Figure 7. Geologic map of the study area	15
Figure 8. Deformation bands in the field	16
Figure 9. Field data and transect locations – Transects #1-8.....	18
Figure 10. Field data and transect locations – Transects #9-12.....	20
Figure 11. Field data and transect locations – Transects #13-16.....	22
Figure 12. Compilation of cumulative thickness plots and stereonet.....	24
Figure 13. Field photos of deformation bands near salt wall contacts.....	26
Figure 14. Field photos of deformation bands near fault surfaces.....	27
Figure 15. Field photos of conjugate sets on deformation bands	28
Figure 16. SEM photos	30
Figure 17. SEM photos	32
Figure 18. SEM photos	33
Figure 19. Compilation of cumulative thickness plots	37
Figure 20. Results from the simplified conceptual finite element model (CM1)	41
Figure 21. Structural evolution of the contractional fold segment in the RS2 model	43
Figure 22. K (horizontal/vertical stress ratio) condition for the RS2 model	44
Figure 23. Finite plastic strain evolution of the downdip diapir in the RS2 model.....	46
Figure 24. Structural evolution of northern Salt Valley	48

1. INTRODUCTION

Many of the largest hydrocarbon reservoirs in the world are found in contractional fold belts, where salt or overpressured mud has mobilized to form diapirs and influence basin structural evolution (e.g., Perdido fold belt, Atwater fold belt, Zagros fold-thrust belt, Niger delta, Kwanza basin; Fiduk et al., 1999; Sepehr and Cosgrove, 2004). In many salt systems, salt diapir development has traditionally been viewed as either passive or reactive, wherein salt flows in response to gradients in sedimentary overburden thickness to produce progressively thickening onlapping sequences or rises toward the surface in response to extension of the sedimentary cover, respectively. Active salt diapirism, wherein salt is interpreted to actively drive deformation of wall and cover rocks, is less commonly considered as a dominant mechanism in diapir formation.

A number of recent numerical modeling studies, however, have demonstrated that mobilized and pressurized salt is not only strong enough to actively deform cover and wall rock sequences and drive second-order reactive diapirism in the arching cover sequences above rising diapirs, but active diapirism may actually be the dominant mechanism of diapir formation in many contractional systems (Nikolinakou et al., 2017; Thigpen et al., 2019). In the numerical models, salt is shown to have the ability to actively “tunnel” through overburden sequences, driving pervasive deformation of wall and cover rocks (Thigpen et al., 2019), which may even lead to seismically-resolvable thinning of overburden sequences to produce the thinned flanks commonly interpreted to result from passive diapirism (Nikolinakou et al., 2017). However, if these models accurately represent diapir evolution in contractional systems, these deformation gradients, which are likely to be sub-seismic in scale, should be preserved in the wall and cover rocks. These gradients may be manifested as brittle deformation in Mohr-Coulomb materials or as plastic sediment compaction and/or even as cataclastic deformation bands in weakly-cemented or uncemented materials. Such plastic deformation is notorious for driving reduction of porosity and permeability of hydrocarbon or water reservoir host rocks, leading to baffling of flow in potential reservoirs (Antonellini and Aydin, 1995; Shipton et al., 2002; Crawford 1998; Vajdova et al., 2004; Ogilvie and Glover, 2001; Ballas et al., 2015). Therefore, in addition to understanding the mechanisms driving diapir evolution in contractional systems, the ability to predict where this salt-related

damage has occurred in wall and cover sequences adjacent to salt is critical for hydrocarbon exploration and production.

In the models of Thigpen et al. (2019), regional strain gradients are predicted in wall and cover sequences proximal to active salt diapirs. This results from both primary active diapirism and secondary reactive diapirism in response to arching of the cover sequences above the rising diapir. To test these model predictions, it is necessary to identify an ideal laboratory that has the potential to preserve evidence of such features. In the Paradox Basin of eastern Utah (Fig. 1), multiple breached anticlinal salt valleys have been produced by differential weathering that has exposed outcrops of high-porosity Cretaceous-Jurassic sandstone on the flanks of these previously active salt diapirs, now dissolved and removed by erosion. The development of these relatively large diapirs (4-5 km tall) is interpreted to have been driven by differential sediment and salt flow (Hudec and Jackson, 2007). This differential loading, which began when sediments were shed off the emerging Uncompahgre uplift during Permian times, initiated regional southwest directed salt flow. Progressive sedimentary loading continued until the Jurassic, resulting in long wavelength contractional folding of the sedimentary packages and development of the salt-cored anticlinal valleys throughout the basin. Both plastic and brittle deformation is observed in sedimentary wall rocks proximal to these salt wall contacts, and the exceptionally well exposed pavement outcrops provide ideal areas to examine the spatial distribution of strain preserved here. This is particularly true for the Salt Valley anticline, in the northwestern part of the basin (Fig. 2). The primary objective of this study is to document the intensity and spatial distribution of strain in wall rocks and cover sequences and use this data to interpret the driving mechanisms of deformation and the related chronology of these events. These results can then be compared to the deformation gradients predicted by numerical models salt diapir evolution.

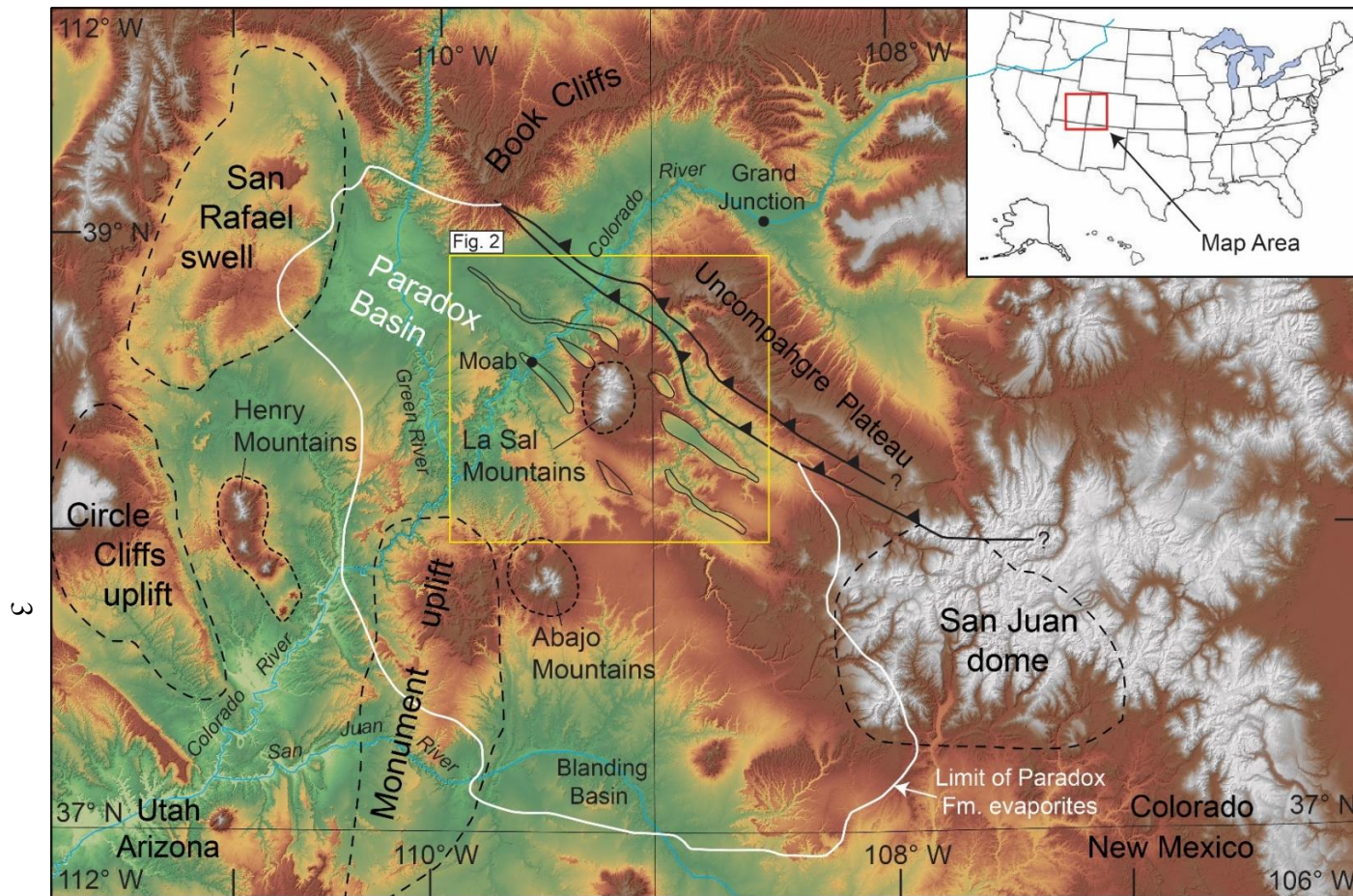


Figure 1. Regional map of the Paradox Basin and surrounding areas. The Paradox Basin, defined as the limit of evaporite deposits assigned to the Paradox Formation, is outlined in white. Structural highs created by uplift are outlined with longer dashed black lines and mountain ranges created by Tertiary igneous intrusions are outlined with shorter dashed black lines. Reverse faults, represented by solid black lines with triangular barbs on the upthrown block, mark the border between the Paradox Basin and Uncompahgre uplift. The extent of the Paradox Basin and adjacent areas were derived from Lawton et al. (2015) Nuccio and Condon (1996) and the digital elevation model shown here. The location of Figure 2 is outlined with a yellow box, and the thin black lines within this area outline anticlinal salt valleys where salt of the Paradox Formation is either exposed or is interpreted to be very near the modern surface. Since the Paradox Basin is a Paleozoic sedimentary basin that has experienced significant burial, deformation, and exhumation, some of the Paradox Basin appears as modern topographic highs.

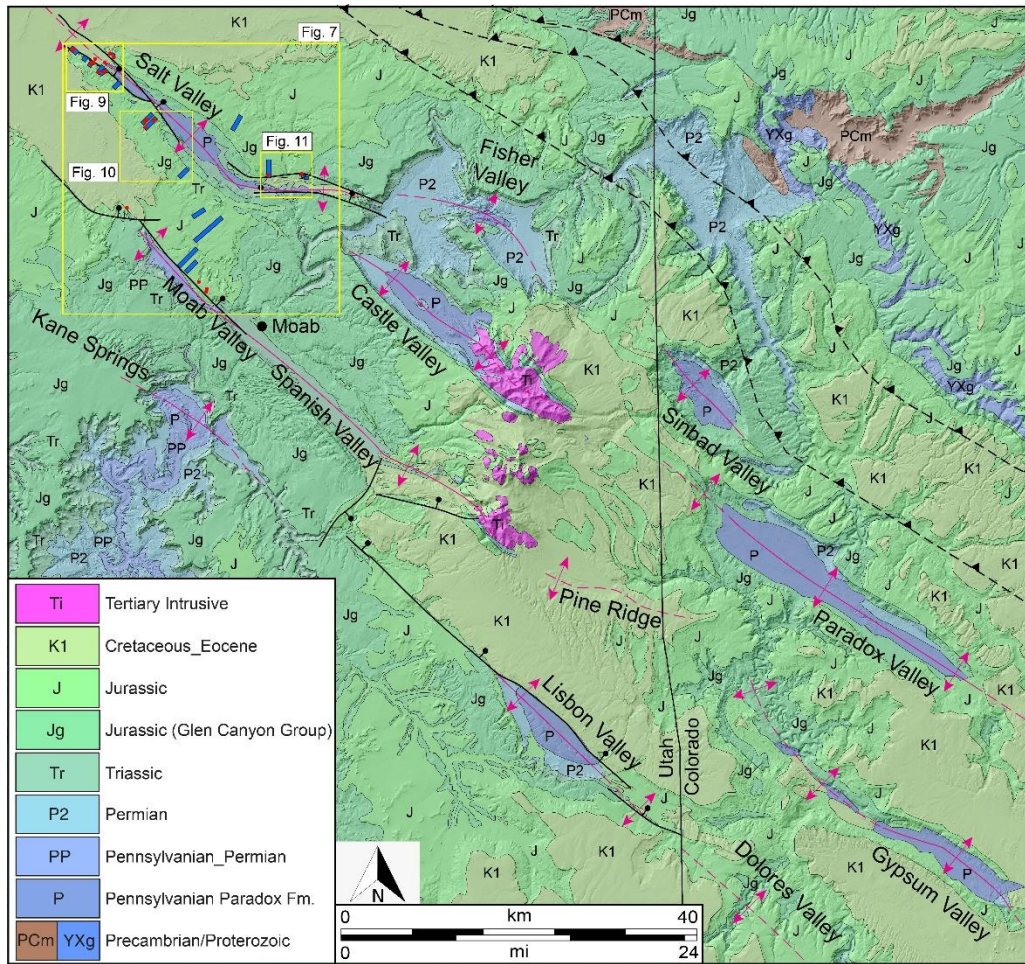


Figure 2. Simplified bedrock geologic map of the northeastern portion of the Paradox Basin. Dashed black lines with triangular barbs on the upthrown block represent the approximate location of the reverse faults in the subsurface, representing the border between the Paradox Basin and Uncompahgre uplift. Solid black lines represent normal faults, with bars on the downthrown block. Anticlinal axes of salt valleys are represented by solid magenta lines (dashed where approximate). The locations of Figures 7, 9, 10, and 11 are outlined in yellow.

2. BACKGROUND

2.1 Evaporite structural systems

Evaporite basins worldwide have zones of complex salt-related deformation, which are caused by the lateral and vertical flow of mobilized salt. On continental margins, flow of the relatively weak salt is commonly gravity-driven, and is generally expressed as updip extensional zones dominated by normal faults that are linked by a common detachment horizon with zones of contractional shortening in the downdip section of the deforming wedge. In the downdip zones, updip extension is accommodated as downdip shortening that can manifest as thrusting, folding, lateral squeezing of preexisting diapirs, or extrusion of salt sheets and salt nappes (Rowan et al., 2004; Fig. 3). Compressional salt systems are also found in foreland fold-thrust belt settings, such as the Zagros in Iran (Sephehr and Cosgrove, 2004), the Sierra Madre Oriental and La Popa basin in northeastern Mexico (Lawton et al., 2001), and the Paradox basin of eastern Utah (Doelling et al., 1988), among others.

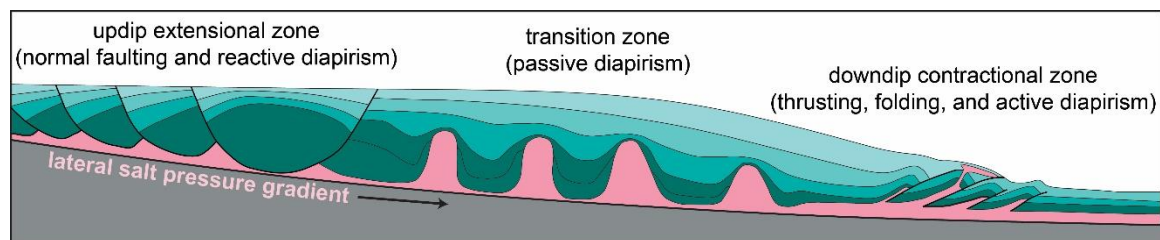


Figure 3. Schematic diagram of a continental margin scale gravity-driven, linked updip extensional and downdip contractional salt system separated by a transition zone. Normal faulting in the updip extensional zone and folding and thrust faulting in the downdip contractional zone are kinematically linked along a common master detachment in the relatively weak basal salt. Modified after Rowan et al. (2012) and Thigpen et al. (2019).

In these systems, salt flow and related diapirism occur in response to lateral pressure gradients caused by differential sediment loading, and this force can drive deformation of sedimentary overburden and wall rocks in multiple ways (e.g., Hudec and Jackson, 2007), including: (1) reactive diapirism, wherein overburden extension and subsequent thinning initiates diapiric rise and allows salt to move vertically through the overburden sequence (Fig. 4a), (2) active diapirism, wherein salt diapirs actively “tunnel” toward the surface by deforming and displacing overburden and wall rocks (Fig. 4b), (3)

erosional piercement, which occurs when overburden is erosionally removed to allow a diapir to emerge (Fig. 4c), and (4) thrust piercement, wherein salt diapirs are driven toward the surface as part of a thrust hanging wall (Fig. 4d). Ductile piercement occurs when fluid overburden mixes with the diapir roof, producing zones of mixed clastics and salt in the extensional domain present above the diapir (Fig. 4e). Passive diapirism, which is also known as downbuilding, occurs when strata onlap the flanks of diapirs exposed at the surface and sediments can accumulate on the salt wall border as the diapir grows (Fig. 4f). In addition to driving deformation of wall and cover rock sequences, all of these mechanisms can exert fundamental controls on sediment distribution patterns and thus control sediment thickness variations across the basin (Baars and Stevenson, 1981).

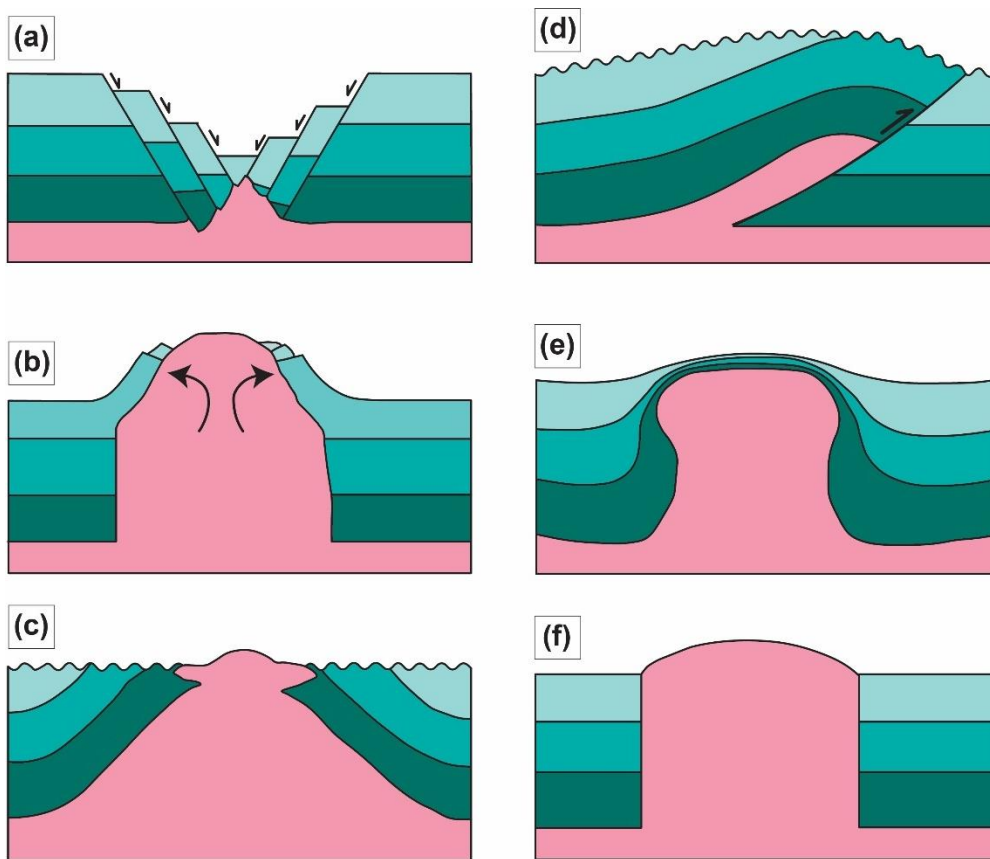


Figure 4. Schematic cross sections of different diapir styles, including (a) reactive piercement, (b) active piercement, (c) erosional piercement, (d) thrust piercement, (e) Ductile piercement, and (f) passive downbuilding. Modified from Hudec and Jackson (2007).

Given the relative mechanical weakness of salt compared to most wall rock and overburden materials (e.g., Davis and Engelder, 1985), most studies consider salt diapirism to be unable to drive pervasive plastic deformation in wall and cover rocks. Salt, mostly in the form of halite with lesser gypsum and sylvite, deforms as a viscoplastic material by dislocation (dry) or diffusion (wet) creep at near surface conditions (Weijermars et al., 1993). However, because diffusion creep is active at a water content as low as 0.05 wt.% and most natural evaporite units contain 0.1-1.0 wt.% water, salt is interpreted to deform dominantly by diffusion creep under most conditions (Weijermars et al., 1993). Salt has an approximate density of $2,200 \text{ kg/m}^3$, and is relatively incompressible; because of this, salt has a complex buoyancy relationship with sedimentary sequences in many basins, as it tends to be denser than recently deposited, uncompacted sediments (bulk density = $1900\text{-}2100 \text{ kg/m}^3$) but become less dense than those sediments (bulk density = $2300\text{-}2650 \text{ kg/m}^3$) as they are progressively buried and compacted (Weijermars et al., 1993). Once salt transitions to being less dense than the surrounding sediments during burial, it becomes buoyant, which creates halostatic instabilities and leads to the rise of diapirs (Hudec and Jackson, 2007).

Recent work from Nikolinakou et al. (2017) and Thigpen et al. (2019) used forward finite element models simulating diapir evolution to demonstrate that these halostatic instabilities can drive major pervasive strain in the surrounding units. The extent and intensity of strain imposed on wall rocks and cover sequences depends on the distribution of sediment and salt in the system, as well as the scale and geometry of the developing diapirs. In the RS2 model of Thigpen et al. (2019), the salt diapir actively “tunnels” through the cover sequence in the downdip compressional end of the linked extensional-contractional system, driving both contractional strain in the adjacent wall and cover rocks and extensional strains in the doming sequence above the rising diapir. Immediately adjacent to the ~ 1 km wide modeled diapir, a plastic strain gradient with finite strain magnitudes $>250\%$ develops within a few hundred meters of the salt wall and strains $>50\%$ are predicted up to ~ 3 km from the diapir wall. Similar finite element models produced by Nikolinakou et al. (2017), which simulate the development of megafaults seen in many salt systems, also produce plastic strain gradients in the wall and cover sequences, with strain magnitudes $>300\%$ within 100s of meters of the salt wall

and strain magnitudes >50% at ~4 km from the diapir. In the Nikolinakou et al. (2017) study, it also shown that, due to the diapir-scale plastic strain that fundamentally changes the layer geometries, kinematic restoration of the final deformed state model was not possible using standard line length techniques, as line lengths are not preserved whilst the plastic strain actively thins and deforms the adjacent wall and cover rocks. However, despite both numerical modeling studies making very similar predictions, such deformation gradients have never been clearly documented in the field.

2.2. Strain accommodation and pervasive plastic “damage” in evaporite systems

In Mohr-Coulomb materials (Fig. 5a) in the upper crust, strain is generally considered to be accommodated by brittle fracturing and faulting and, to a lesser degree, by folding. Mohr-Coulomb materials generally deform to failure (faulting and fracturing), and this style of deformation is commonly associated with low porosity rocks, such as granite, basalt, metamorphic rocks, and well-cemented sedimentary rocks. However, it may not adequately describe deformation processes in sedimentary rocks with higher porosities and/or lower levels of cementation (e.g., Schultz and Siddharthan, 2005). In high-porosity (>15%) rocks that are poorly- or uncemented, pervasive plastic strain can be manifested as both matrix compaction/porosity reduction and as accelerated compaction and deformation band formation (Aydin et al., 2006; Fossen, 2010; Fossen et al., 2007; Fossen et al., 2011). This type of material behavior, known as critical state (Wong et al., 1997) (Fig. 5b), differs from classic Mohr-Coulomb behavior in that the material will plastically yield beyond the elastic range rather than fail by fracturing or faulting. In critical-state materials, plastic yielding initially occurs by permanent and irreversible pore collapse and porosity reduction, which acts to strengthen the material (Fig. 5c). This contrasts with Mohr-Coulomb materials, wherein evolution through the elastic range to failure actually reduces the strength of the material to its residual frictional strength, assuming a suitably-oriented stress field (e.g., Schultz and Siddharthan, 2005).

Critical state behavior is commonly illustrated by a “ p - q ” diagram (Fig. 5b and c; Antonellini et al., 1994; Schultz and Siddharthan, 2005), which is defined by an x (p) and

y (q) coordinate axis that represent mean and deviatoric stress, respectively. The mean stress (p) is defined as:

$$p = [\sigma_1 + \sigma_2 + \sigma_3] / 3$$

wherein $\sigma_1, \sigma_2, \sigma_3$ represent the maximum, intermediate, and minimum stress values, respectively. Strictly speaking, the vertical axis (q) is the deviatoric stress however, it essentially reduces to differential stress:

$$q = \sigma^1 - \sigma^3$$

under drained (i.e., non-poroelastic) conditions ($\sigma_1 - \sigma_3$). The value of q equals the diameter of the Mohr circle and relates shear stress to a given value for mean stress (p ; Schultz and Siddharthan, 2005). The critical state yield envelope is defined as a primary yield function (Φ) and plastic potential (Ψ) using a smooth three-invariant surface that intersects the hydrostatic axis in both tension and compression:

$$\Phi(\sigma, \varepsilon_v^p) = g(\theta, p)q + (p - p_t) \tan \beta \left(\frac{p - p_c}{p_t - p_c} \right)^{1/n}$$

$$\Psi(\sigma, \varepsilon_v^p) = g(\theta, p)q + (p - p_t) \tan \Psi \left(\frac{p - p_c}{p_t - p_c} \right)^{1/n}$$

where p is the effective mean stress; q is the deviatoric stress; θ is the Lode angle; p_t is the tensile intercept of the yield surface with the hydrostatic axis; p_c is the pre-consolidation pressure or compressive tensile intercept of the yield surface with the hydrostatic axis; β and n are material constants which define the shape of the yield surface in the p - q plane; and $g(\theta, p)$ is a function that controls the shape of the yield function in the deviatoric plane (Crook et al., 2006).

In practice, critical-state materials actually have two yield surfaces, which define distinct zones of material behavior, including: (1) the elastic range below the sub-yield

envelope, in which all deformation is recoverable, (2) the sub-yield envelope, which indicates the conditions at which pore collapse and porosity reduction will occur, leading to finite strengthening of the critical state material and expansion of the sub-yield envelope, and (3) the cataclastic yield envelope in which the onset of cataclastic grain crushing and deformation band formation occurs. Although porosity reduction is a form of critical state yielding that generally precedes deformation band formation, porosity reduction cannot be directly measured along transects in the field, and thus this study chose to use mesoscopic deformation band occurrence as a proxy for critical state damage in this study.

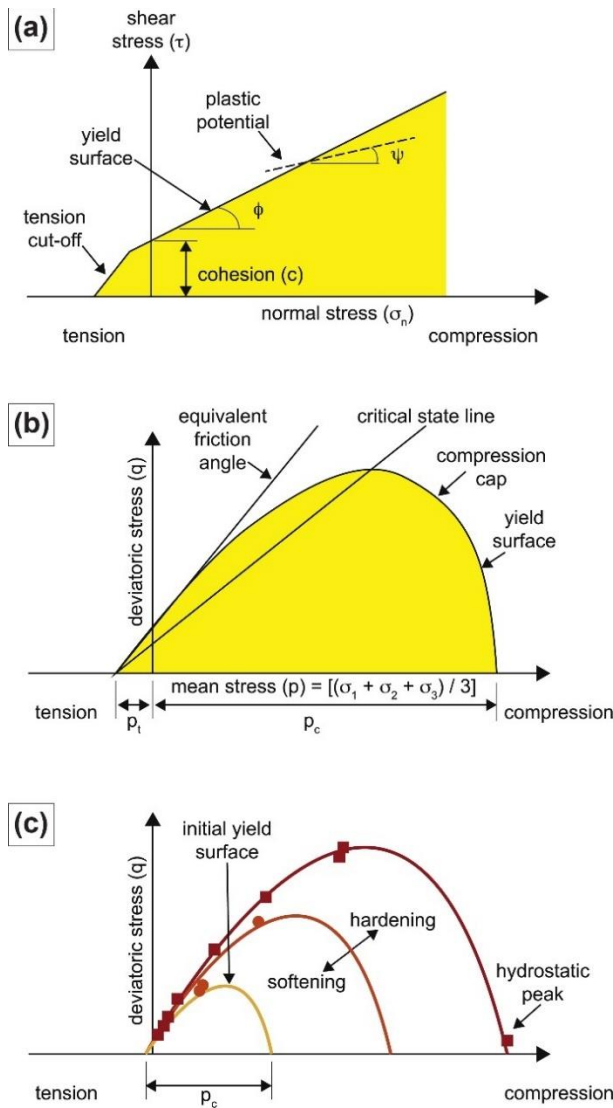


Figure 5. (a) Mohr-Coulomb failure envelopes illustrate the stress conditions for brittle failure of low porosity geologic materials. (b) Plots of p-q space characterize the stress conditions for plastic yielding in critical state materials, such as unconsolidated sediments. Stress conditions along the yield surface to the left of the critical state line create dilation/shear bands, and compaction/shear bands form along the yield surface to the right of the critical state line. (c) Strengthening or weakening of the material occurs as the as the material porosity changes along a finite strain path. Strain softening occurs when the yield envelope decreases in size (moving inward towards the critical state line) and strain hardening occurs when the envelope grows (moving outward towards the critical state line). In practice most materials follow a progressive strain hardening path and rarely is strain softening observed. The hydrostatic peak, also defined as P^* , is a function of the grain size and porosity of the critical state material. Modified from Thigpen et al. (2019).

Although experimental studies are limited, deformation bands in rocks have been created in a laboratory setting by Mair et al. (2000, 2002) and Vajdova et al. (2004) and the experimental data obtained from these studies shows that the number and thickness of deformation bands increase with progressively increasing finite strain (Fig. 6). To quantify strain accommodated by their experiment, Mair et al. (2000) recorded individual bands thicknesses with an optical micrometer, and their laboratory test showed the development of more individual deformation band strands and wider damage zones with increasing axial strain. Because of this, we also consider the accumulation of deformation band thicknesses with higher strain magnitudes as a useful proxy for relative strain values of deformation bands observed in the field, in addition to the number of bands recorded in previous studies (Schueller et al., 2013).

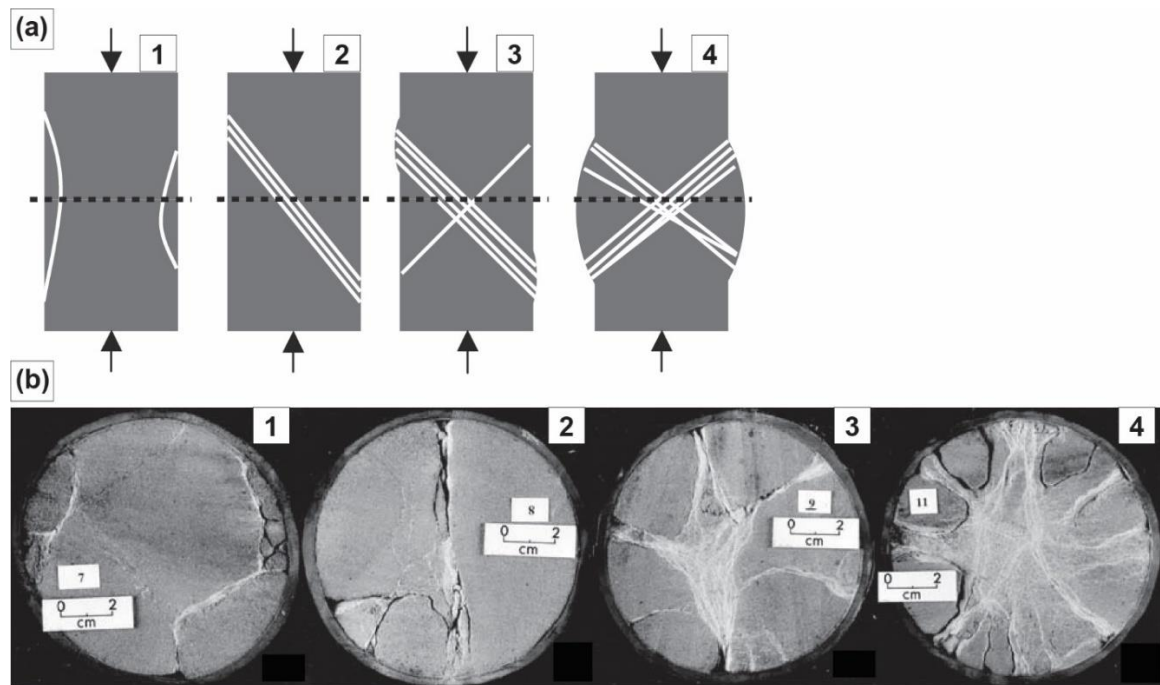


Figure 6. (a) Schematic diagrams illustrating the geometry and distribution of deformation band damage zones created during the triaxial experiments of Mair et al. (2002). Dashed lines represent the cut plane shown in the photographs in (b). (b) Photographs of deformation band arrays created as the Locharbriggs sandstone cores were deformed to 7.8% axial strain under confining pressures of 13.5 MPa, 27.3 MPa, 41.4 MPa, and 54.8 MPa, respectively, from left to right. Modified from Mair et al. (2002).

2.3. Geologic setting of the Paradox Basin study area

The Paradox Basin in Utah preserves multiple breached anticlinal salt diapir structures (Fig. 2) that are flanked by pavement exposures of relatively high-porosity Cretaceous-Jurassic sandstone units. In the Salt Valley, the anticlinal salt dome is flanked by the relatively high porosity Moab member sandstone. Because of the high paleoporosity of these units and the large areal extent of these units, this makes this area an ideal natural laboratory to test whether or not plastic critical state deformation gradients are preserved in the salt wall and cover sequences.

The Paradox Basin is bound to the northeast by frontal thrust faults of the Uncompahgre uplift (Fig. 1). The oldest rocks exposed in the study area are Pennsylvanian evaporites and carbonates of the Paradox Formation (Doelling and Kuehne, 2013), which are commonly preserved in the core of breached anticlinal salt valleys throughout the basin (Fig. 2). Due to flexural subsidence in the northeast portion of the basin, evaporite deposition produced an abnormally thick sequence of mostly halite and gypsum (~1,525-1,825 m) proximal to the Uncompahgre uplift (Baars and Stevenson, 1981). During the Permian, thick (~2,490-4,575 m) packages of Cutler Group sediments derived from erosion of the Uncompahgre highlands were deposited onto the evaporite sequence, which drove overburden loading and initiated development of long wavelength pressure gradients in the underlying evaporite sequences. This is interpreted to have driven southwest-directed flow of the evaporite sequence throughout the basin (Baars and Stevenson, 1966).

Diapirism at Salt Valley likely initiated shortly after, or even during deposition of Paradox Formation salts, as salt began to move laterally to the southwest during the Late Pennsylvanian. Permian diapirism is expressed as lateral thickness variations in Cutler Group rocks. This activity continued into the Late Triassic, which is indicated by Early Triassic Moenkopi Formation sediment packages that onlap the diapir-cored anticlines (Doelling and Kuehne, 2013). Beginning in the Late Triassic, deposition transitions to more uniformly distributed sedimentary packages, which continues through the Early Cretaceous. Deposition of largely aeolian sands continued through most of the Jurassic, with a transition to fluvial and marine shale deposition during the Cretaceous. The influx and retreat of the Western Interior Seaway from ~105-70 Ma (Blakey, 2014) deposited

~1,100 meters of the Mancos Shale, followed by the ~153-287 meters of the Mesa Verde Group (Doelling, 2001). The basin was later uplifted and incised to produce the current topography.

2.4 Deformation band formation in the Salt Valley

On the flanks of the Salt Valley, deformation bands are pervasive in Jurassic sandstones such as the Moab member of the Curtis Formation and the Entrada Sandstone and because of this, a number of studies have examined deformation band genesis in the Paradox Basin (Aydin and Johnson, 1978; Aydin et al., 2006; Berg and Skar, 2005; Fossen and Hesthammer, 1997; Fossen, 2010; Fossen et al., 2011; Johansen and Fossen, 2008; Kolyukhin et al., 2010; Okubo and Schultz, 2007; Rotevatn and Fossen, 2011; Shipton et al., 2002; Shipton and Cowie, 2001; Soliva et al., 2016; Solum et al., 2010; Torabi and Fossen, 2009; Zuluaga et al., 2014). However, few studies have explicitly focused on the deformation band “damage” zones which are pervasive within the Moab member pavement outcrops on the limbs of the Salt Valley anticline. This study examines the spatial distribution and frequency of deformation bands on the flanks of the Salt Valley anticline, with a specific emphasis on identifying the presence or absence of long wavelength strain gradients predicted by the numerical studies. Additionally, this study will emphasize the separation of deformation bands that form proximal to fault planes (i.e., interpreted fault “damage” zones; Ballas et al., 2015; Fossen et al., 2007; Zuluaga et al., 2014; Jackson and Hudec, 2017) and those that form as pervasive distributed plastic damage near salt diapirs, as they may represent different length scales of strain accommodation driven by different mechanisms.

3. METHODS

In order to characterize mesoscopic deformation on the flanks of the Salt Valley, mapping transects normal to the paleo-salt wall were planned in various locations (Fig. 7). The orientation of the transects normal to the paleo-salt wall was chosen to intersect as many deformation bands as possible, as most of those features strike sub-parallel to that salt margin. Additionally, the orientation of these transects provides the best opportunity to characterize any strain gradients that have developed normal to the paleo-

salt wall. Mapping transects targeted the Moab member, which is a high porosity sandstone that is preserved as relatively large pavement outcrops on the flanks of the now eroded salt diapir. Transects were mapped in 63 m intervals using a measuring tape and deformation band location, orientation, and band thickness were recorded (Fig. 8). Because the experimental studies discussed above clearly show that the total strain accommodated in these systems is directly related to both the number of deformation bands and their accumulated thickness, this is why an accurate record of deformation band thicknesses along transects is critical for our study.

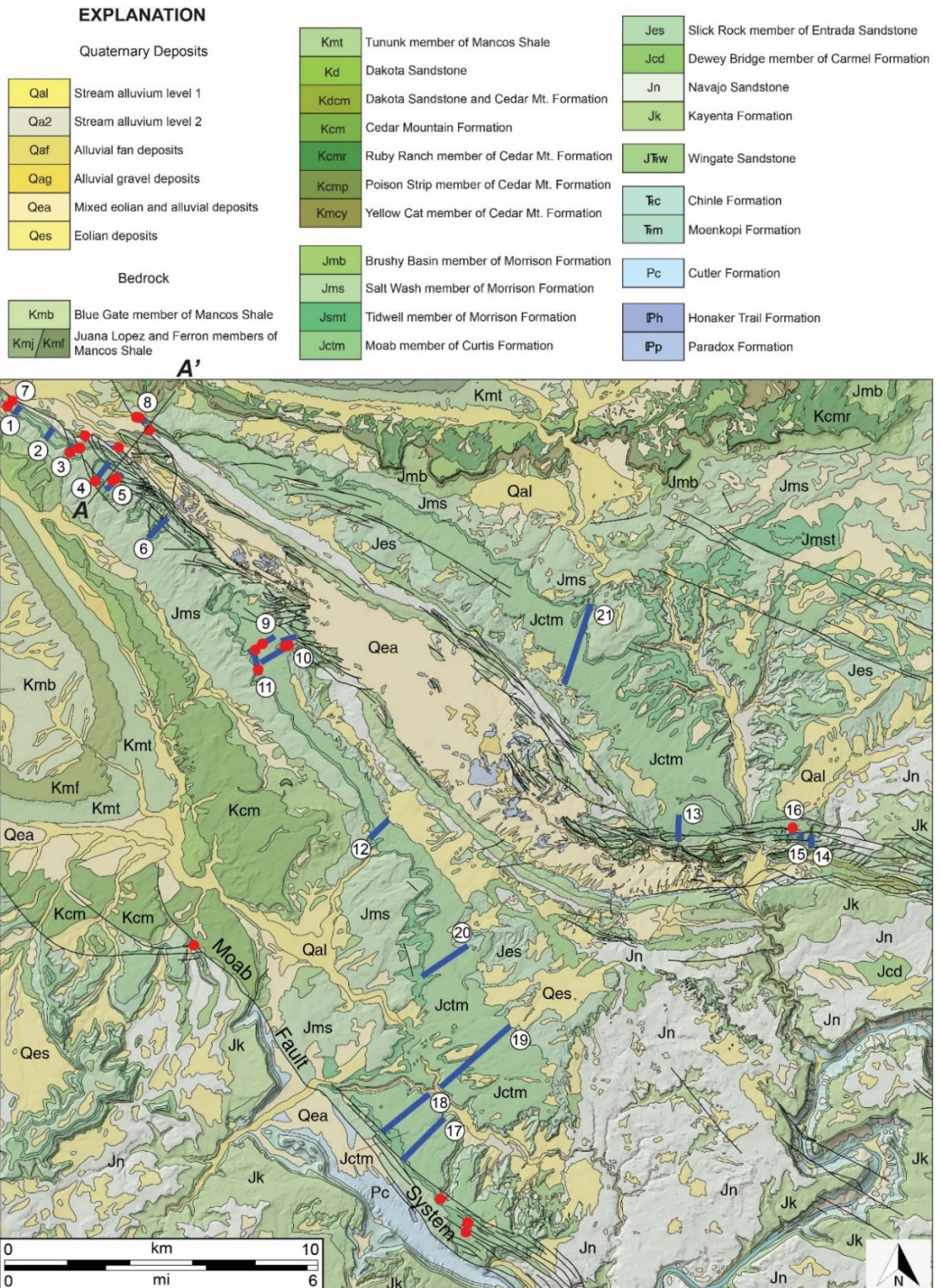


Figure 7. Geologic map of the Salt Valley study area. Bedrock units, surficial deposits and major faults are shown. Oriented hand sample locations are represented by red circles. Transect locations are numbered and are represented by thick blue lines. The cross-section line in the northwest corner (A-A') is the location of the cross section shown in Figure 24.

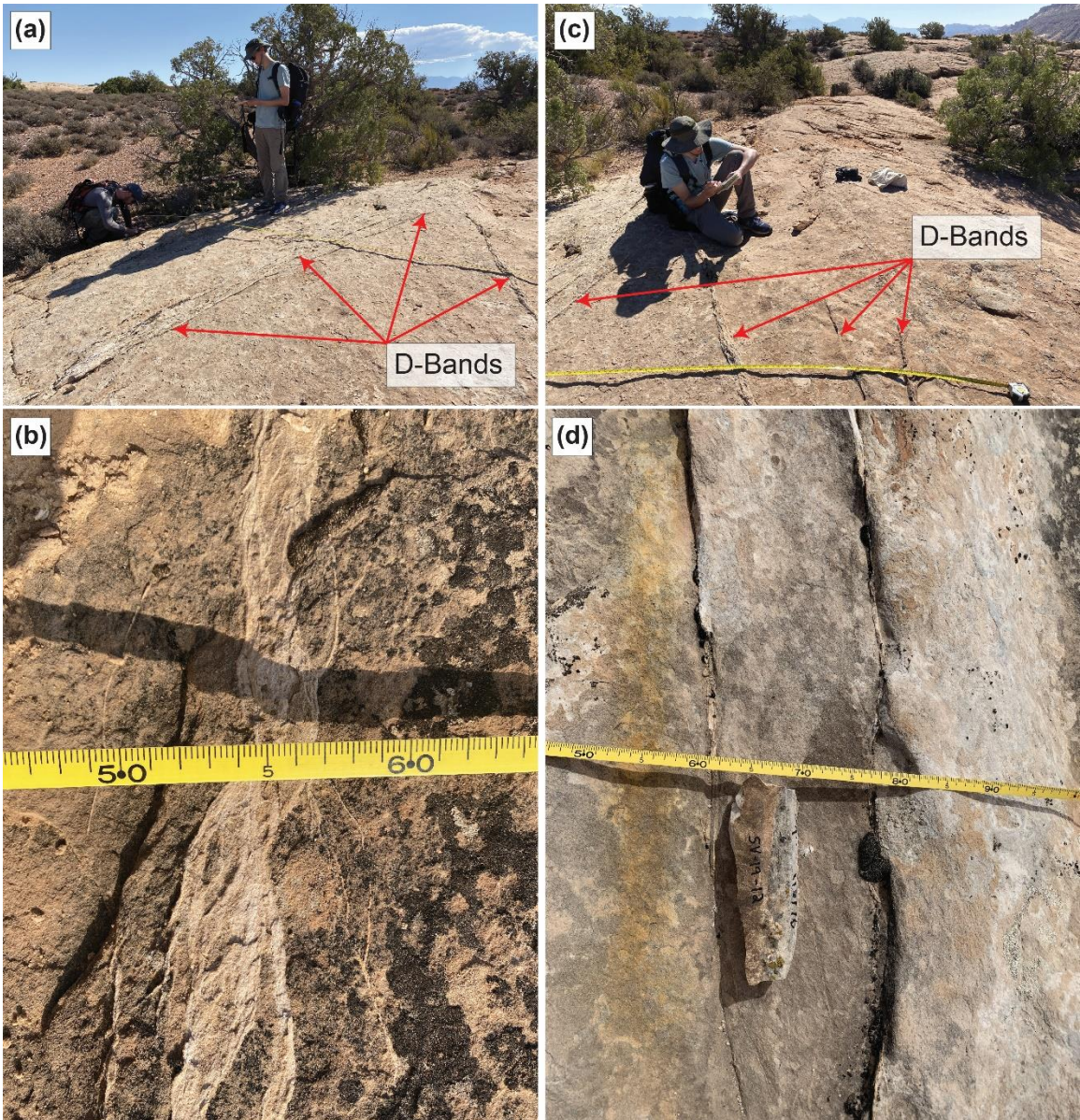


Figure 8. (a) Conjugate deformation band sets exposed in the Moab member pavement. (b) Anastomosing set of thin deformation bands that have coalesced to form a zone of deformation ranging from 2 to 4 centimeters thick. (c) Conjugate set of deformation bands, with approximately 30 degrees difference in the strike of the set of deformation bands near the center of the photo and the set of deformation bands entering the photo from the bottom left. (d) Multiple oriented samples were collected along transects.

Multiple oriented hand samples were also collected along transects in order to produce polished thin sections for petrographic and scanning electron microscope (SEM) analysis. Oriented samples included units that contain deformation bands, units within fault damage zones, units near salt wall contacts, and at locations 100s to <1,000 meters

from mapped faults or salt wall contacts that could be used as control (undeformed host rock) analyses (Fig. 7). Using the SEM, images were captured using backscattered electron detection (BED-C), secondary electron detection (SED), and cathodoluminescence (CL). SEM analysis allows for the characterization of the deformation bands at a finer resolution than is possible with a petrographic microscope and CL allowed us to differentiate the relative age of overprinting veins and cements. Additionally, energy dispersive X-ray spectroscopy (EDS) was used to mineralogically classify all clasts, matrix phases, and cements.

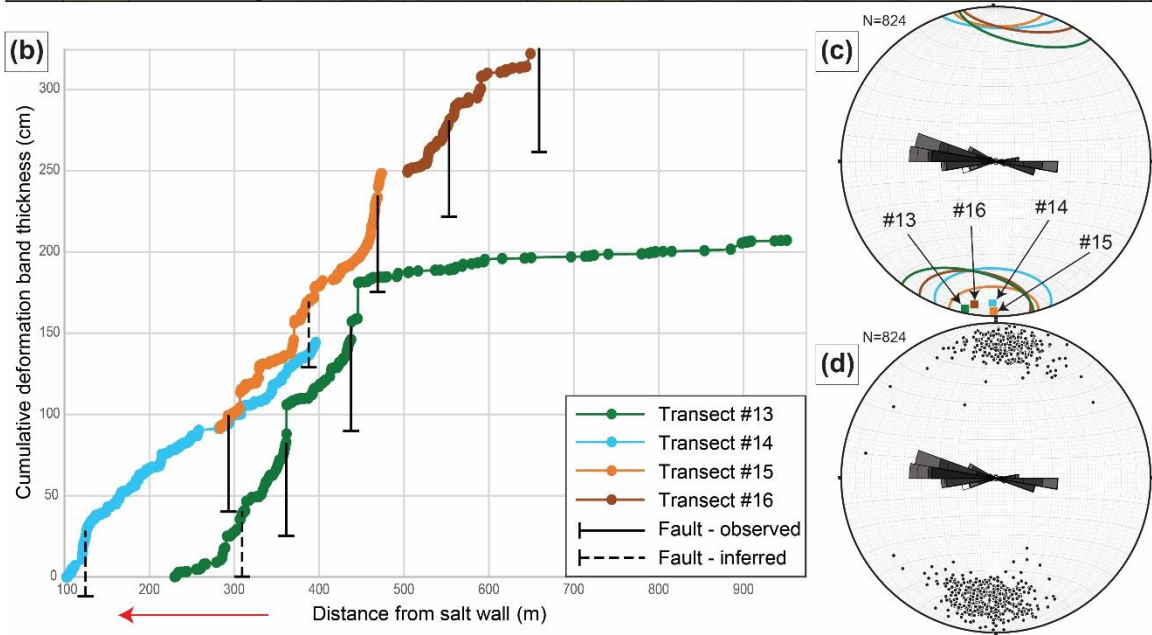
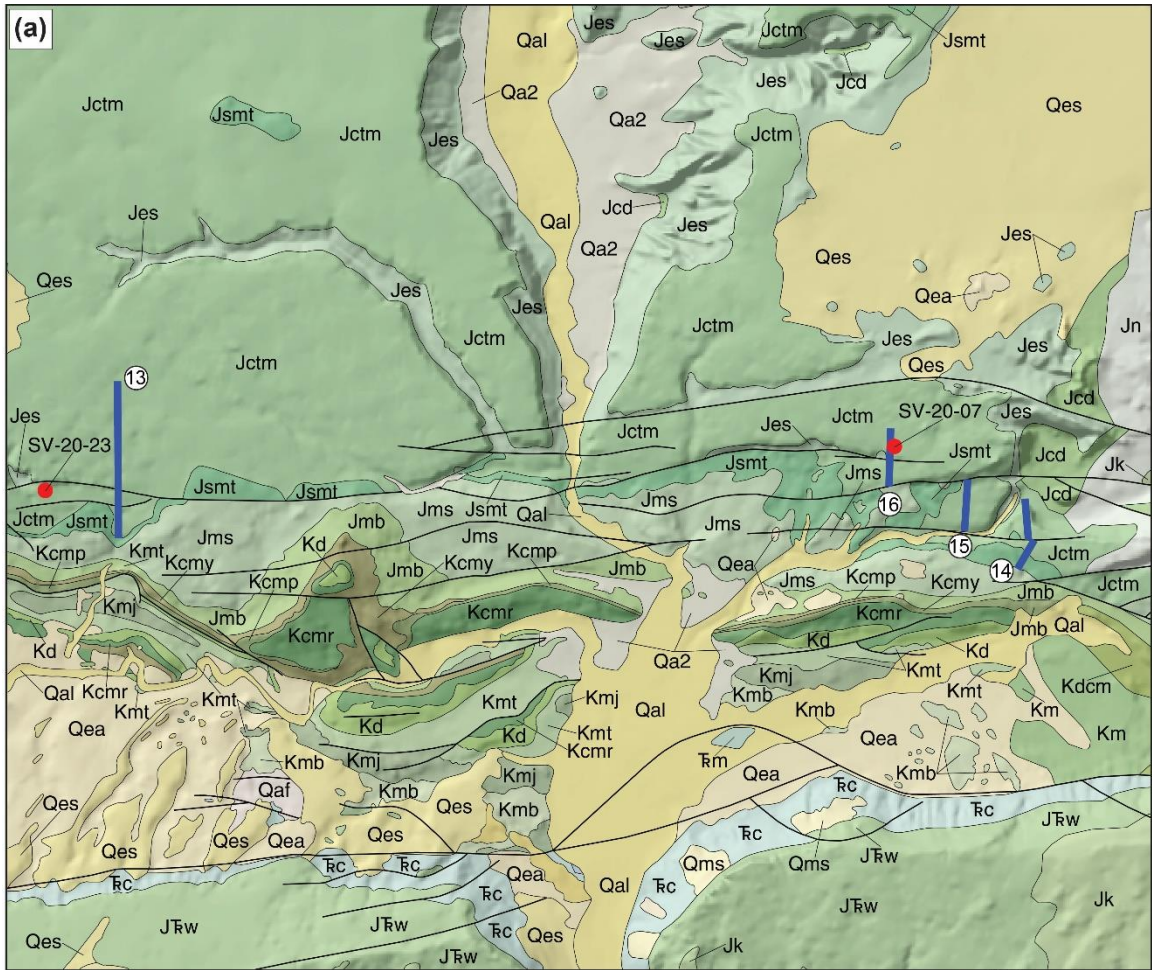
4. RESULTS

4.1. Mesoscale structural transects

The results of all mesoscale structural transects are shown in Figs. 9-12. Deformation bands within the study area are predominately compactional, with variable amounts shear. Deformation planes strike roughly parallel to the anticlinal axis of Salt Valley (90-135°) and generally dip between 60-70°. Dip values often appear steep to nearly vertical in outcrop but in many of the pavement exposures, the geometry of dip surfaces are obscured; these instances are recorded as vertical and are not included in the data shown in stereonet plots. With few exceptions, most structural transects preserve numerous mesoscopic deformation bands. Band thickness accumulations display two main trends. A long wavelength (1-3 km) decrease in deformation band thickness accumulation per unit distance occurs with increasing distance from the salt wall and/or the anticlinal axis of the salt dome. Within this longer wavelength trend, a shorter wavelength (<1-50 m) trend was observed wherein band thickness accumulation increases substantially in the vicinity of mapped fault zones.

Figures 9. (a) Geologic map of the Valley City area to the north of Klondike Bluffs (location shown in Fig. 2). Transect locations (blue lines) and sample localities (red dots) are shown. (b) Plot of cumulative deformation band thickness (y-axis, cm) with distance from the Salt Valley salt wall (x-axis, m). Observed faults were either directly observed in the field or previously mapped and inferred faults are locations where the steeper gradient of deformation band accumulation may indicate that a fault is present, but no fault was observed in the field. (c-d) Stereonets of deformation band orientation data for (c) transect 3 and (d) transects 2 and 4, with rose plots for strike (gray polygons), poles to planes (black circles), and conical best fit representation (colorized to match data on the graph).

Figures 10. (a) Geologic map of the Klondike Bluffs area (location shown in Fig. 2). Transect locations (blue lines) and sample localities (red dots) are shown. (b) Plot of cumulative deformation band thickness (cm, y-axis) with lateral distance from the Salt Valley salt wall (m, x-axis) for transect 11. (c-d) Stereonets of deformation band orientation data for (c) transect 10 and (d) transect 11. Stereonet symbology is the same as Figure 9.



Figures 11. (a) Geologic map of the Fiery Furnace and Delicate Arch area (location shown in Fig. 2). Transect locations (blue lines) and sample localities (red dots) are shown. (b) Plot with cumulative deformation band thickness (cm, y-axis) with lateral distance from the Salt Valley salt wall (m) on the x-axis. Observed faults were either directly observed in the field or previously mapped and inferred faults are locations where the steeper gradient of deformation band accumulation may indicate that a fault is present, but no fault was observed in the field. (c-d) Stereonets of deformation band orientation data for transects 13, 14, 15, and 16, with (c) conical best fit for each transect and (d) poles to planes of all transects combined. Stereonet symbology is the same as Figure 9.

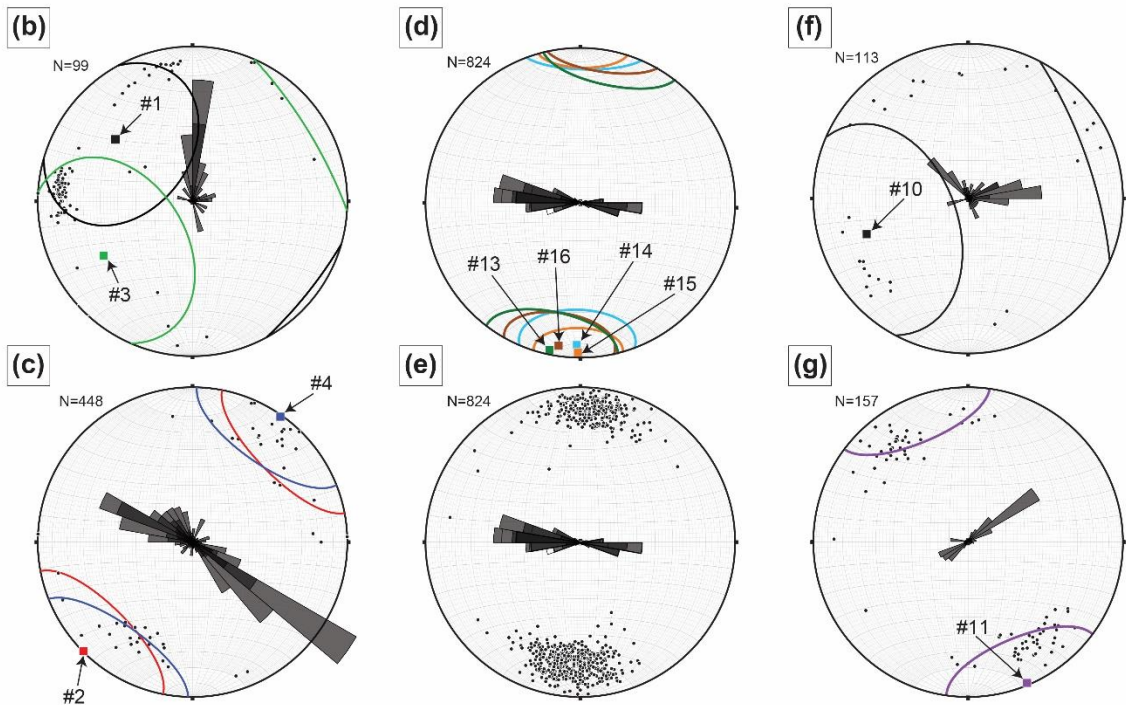
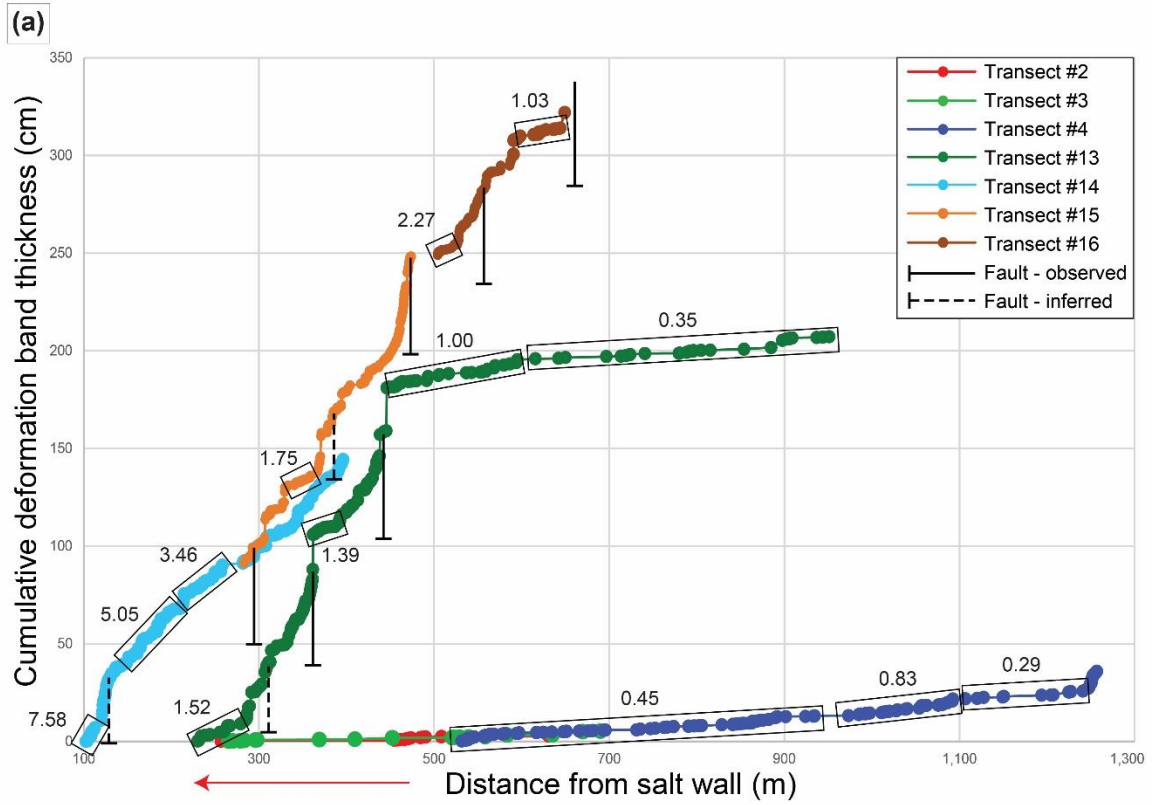


Figure 12. (a) Compilation of cumulative deformation band thickness plots shown in Figures 9–11. Sections of data that are interpreted to define the long wavelength gradient (i.e., outside of the fault “damage” zones) are shown (black boxes) with calculated values of deformation band thickness accumulation (mm) per lateral meter of transect distance.

The long wavelength trend shows a decrease in the rate of deformation thickness accumulation with increasing distance from the paleo-salt wall. Immediately adjacent to the paleo-salt wall, porous sandstone units (i.e., Moab member and isolated Morrison Formation sandstone units) preserve incredibly dense zones of plastic deformation, with 160-186 (mm)_D/m (millimeters of deformation band thickness accumulation per lateral meter) (Fig. 13). Such dense zones of deformation banding proximal are typically observed either within 10-30 meters of the paleo-salt wall on the anticlinal flanks or in “roof pendants” of cover sequence rocks that now directly overlie the Paradox salt units in the valley floors. Moving away from the salt wall, deformation band accumulation rates drop from several centimeters of deformation band thickness accumulations per meter to rates of ~7.6 (mm)_D/m at ~100 meters from the paleo-salt wall. This decreases further to 5.05 (mm)_D/m at 150-200 meters, 3.46 (mm)_D/m at 200-275 meters, and then from ~2.0 to 1.0 (mm)_D/m at distances of 300-500 meters. Deformation bands eventually become absent at distances ranging from ~1,500-2,800 meters away from the salt wall and into the valley syncline axis between adjacent salt valleys.

Within this long wavelength trend of deformation band accumulation, the short wavelength trend (~1-20 m lateral distance) appears as localized peaks in deformation band accumulation and proximal to observed or inferred brittle faults. This short wavelength trend of increased cumulative deformation thickness within meters of fault planes is clearly apparent in multiple transects (Fig. 12). Deformation bands proximal to faults are often anastomosing sets running roughly parallel to these faults and typically dissipate within a few meters of the brittle displacement plane (Fig. 14). As is common in many brittle fault systems, most of these fault planes preserve slickenlines that show the normal slip motion. Faults with higher displacement magnitudes are typically associated with larger total accumulations of deformation band thickness (Fig. 11). These observations are similar to those Schueller et al. (2013), wherein the density and distribution of deformation bands is primarily dependent on the throw of the fault, and there is an exponential drop in the number of deformation bands with increasing distance from the fault planes.

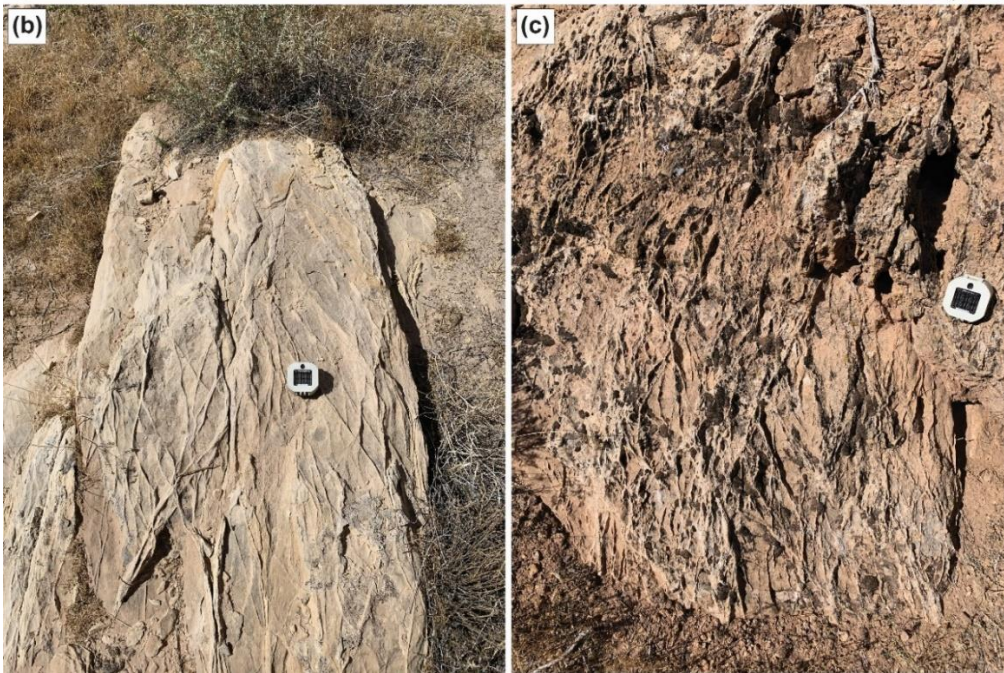
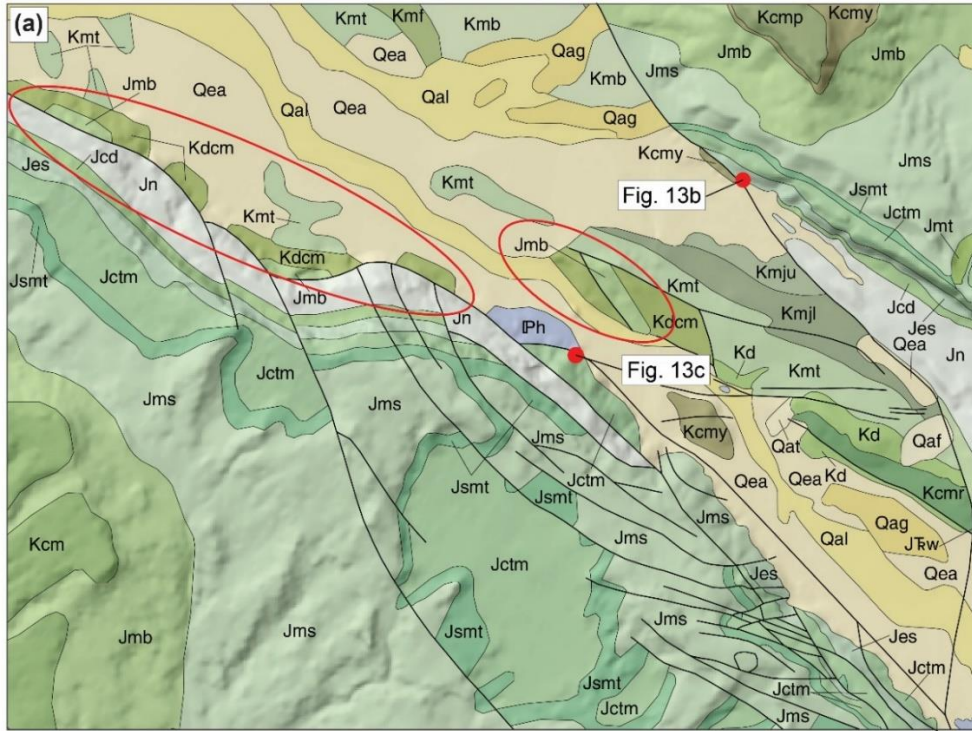


Figure 13. (a) Geologic map of the Valley City area showing the locations of outcrops with intense deformation banding immediately adjacent to the paleo-salt wall, and Morrison Formation roof pendants (red ellipses) (b) Intense deformation banding on the northeaster flank of the Salt Valley ~25 meters from the interpreted paleo-salt wall. Outcrop yields 14.6 cm of deformation band accumulation over a distance of 91 cm ($160 \text{ (mm)}_D/m$). Deformation planes dip $\sim 65\text{-}85^\circ$ and strike roughly parallel to Salt Valley anticlinal axis. (c) Intense deformation banding on the southwest flank of the Salt Valley, ~5 meters from the interpreted position of the paleo-salt wall. Outcrop yields 12.1 cm of deformation band accumulation over a distance of 65 cm ($186 \text{ (mm)}_D/m$).

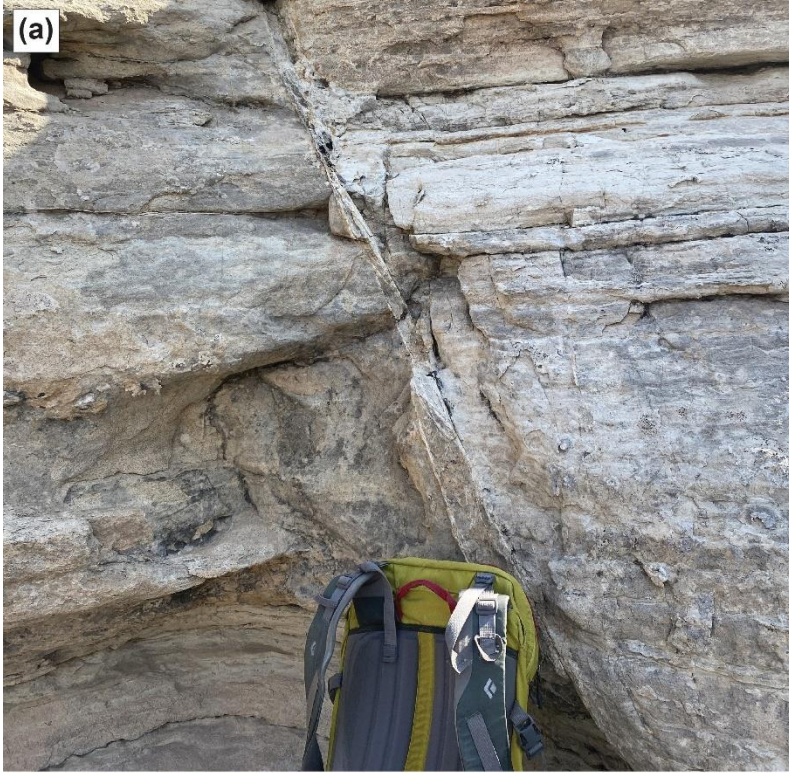


Figure 14. (a) Anastomosing compactional deformation bands that run roughly parallel to a small offset fault (~8-10 cm) and are only visible within centimeters of the fault plane. (b) Deformation bands near a similar type of fault (offset ~2-3 cm) which are also only observed within several centimeters of slip surfaces.



Figure 15. Outcrop photos of conjugate deformation band sets on the flanks of the Salt Valley anticline. (a) Several conjugate sets within view, which are best exposed in the upper left of the photo. Horizontal length of the outcrop running through the center of the photo is ~25 meters. (b) Two conjugate sets of deformation bands located ~70 meters from the Salt Valley salt wall (blue 40-liter backpack for scale). (c) Single conjugate set of deformation bands (outcrop ~1 meter tall). (d) Wide angle conjugate set of deformation bands (outcrop ~10 meters tall).

4.2 Petrographic and SEM analyses

SEM analyses of samples collected along transects were used for microscopic examination of deformation bands and their host matrix material. Samples containing deformation bands are composed predominantly of rounded quartz grains with grain diameters of 50-300 μm , with lesser potassium feldspar (typically ~2-5%) and zircon (<1%). In deformation bands, quartz grains show variable amounts of grain crushing and cataclasis, and limited potassium feldspar grains show similar damage. Cement composition in these units varies across the study area, but these samples generally yield current preserved (uncemented) porosities of 16-37%, with much of the matrix porosity now filled with calcite cement and lesser amounts of barite, Fe oxide, Ti oxide, kaolinite, and malachite cement. These samples have varying degrees of weathering and thus the amount of cement preserved varies by sample. Cemented porosity measurements taken from the general matrix of host rocks, range from 7-14% in samples where calcite cement is mostly preserved (e.g., Fig. 16a and e). Kaolinite cement is typically present at <2%; however, sample SV-20-23 is composed of ~20% kaolinite. Some samples have higher amounts of what are typically trace minerals in their cement; these include samples SV-19-06, SV-19-07, SV-20-03, SV-20-11, and SV-20-21 (5-10% Fe oxides) samples SV-20-15 and SV-20-19 (5-10% barite) and sample SV-20-16 (~15% malachite).

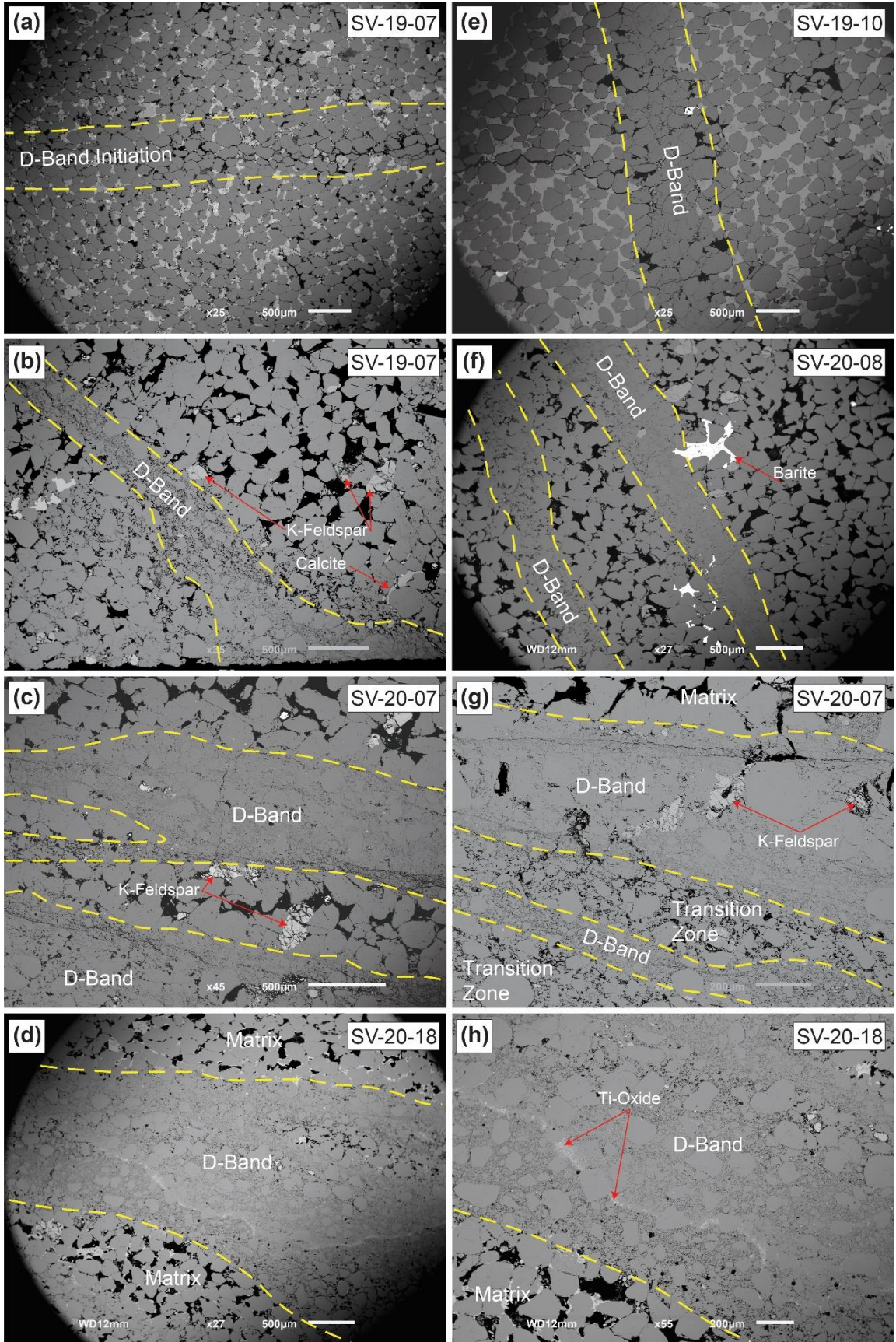


Figure 16. SEM backscatter electron detection (BED-C) images of selected samples, showing the varying styles of deformation bands in Salt Valley. (a) Some bands show minor grain crushing, with plastic strain accommodated via localized pore collapse. This feature could not be observed in hand sample. (b) Shows further grain crushing with more cataclasis; this deformation band, and those in (c-h) are large enough to be visible in hand samples. Microstructural analysis of all the samples shows that samples SV-20-07 (c and g) and SV-20-18 (d and h) are samples with the highest degree of cataclasis and were collected ~1,000 meters and ~1,750 meters from the Salt Valley salt wall, respectively, and 65 meters and 370 meters from the nearest observed faults, respectively (see Figs. 10 & 11).

All deformation bands analyzed in this study are classified as compaction bands, with significant variation in the degree of pore collapse and grain cataclasis between samples (Fig. 16). As the degree of cataclasis increases, deformation band thickness tends to increase, and comminution occurs, decreasing average grain size, and forming ultracataclastic deformation bands composed of primarily quartz (e.g., Fig. 16d & 16h). Where detrital K-feldspar grains are involved in the deformation band damage zones, they also show substantial cataclasis (Figs. 16-18). Porosity in deformation band damage zones is substantially lower than the surrounding host matrix and can be as low as 1-2% (e.g., cataclastic zones in Fig. 16). As discussed above, the host rock in most samples typically contains calcite cement, with lesser barite and Ti- and Fe-oxide cements (Figs. 17f and 18e-h). Importantly however, these cements are rarely deformed inside the deformation band damage zones and where present in these zones, they fill voids and fractures that cross-cut the deformation bands (Figs. 17d & 18e).

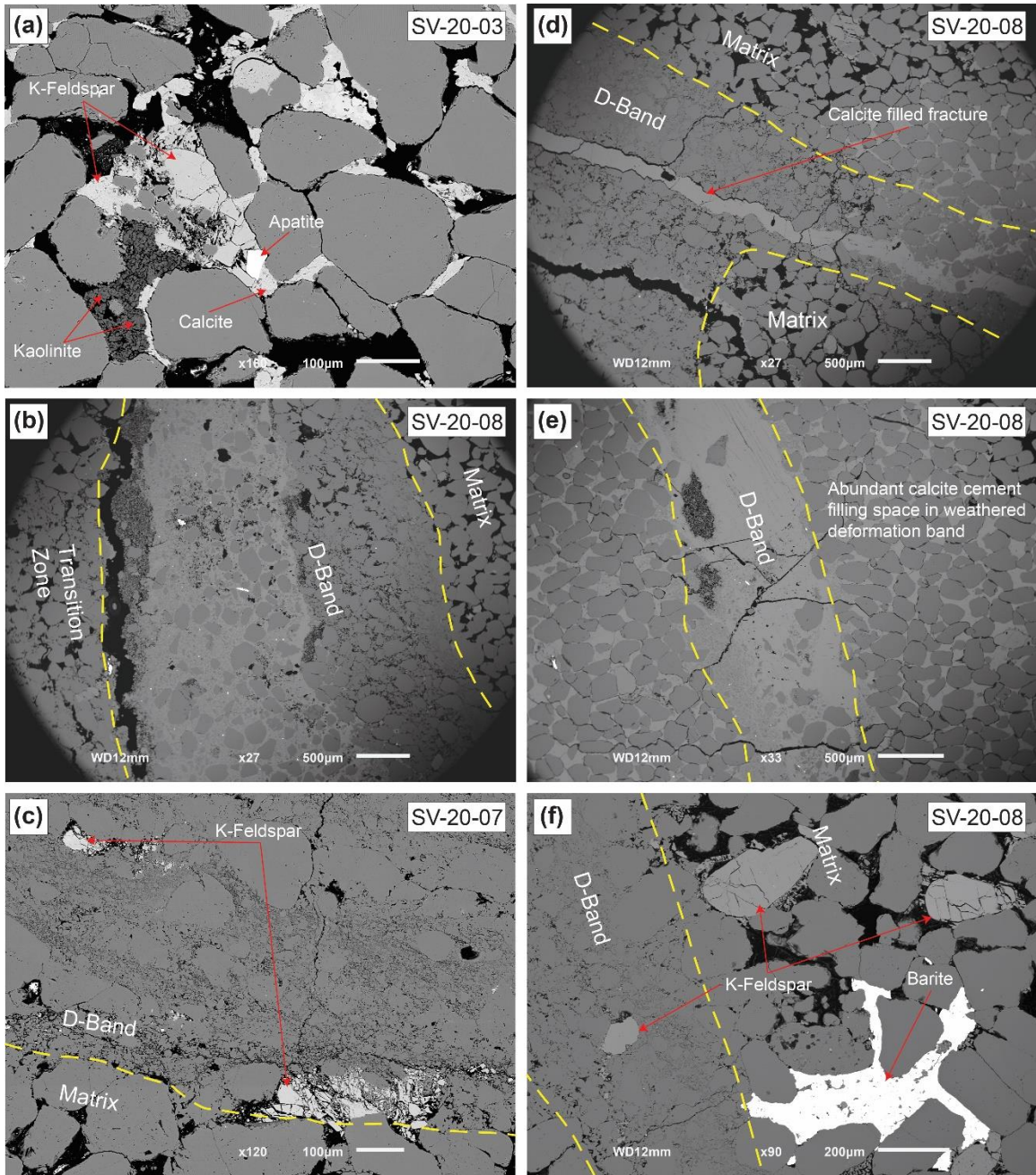


Figure 17. SEM photos collected using backscatter electron detection (BED-C). Mineral phases were identified using X-ray spectroscopy (EDS). (a) Fractured quartz and K-feldspar grains are surrounded by matrix calcite and kaolinite cements, and apatite, which show no evidence of fracturing. (b) (b and e) Damaged quartz within calcite cement. (c) Heavily damaged potassium feldspar grains on the periphery a deformation band with cataclasis. (d) Fractured deformation band is filled with calcite cement. (f) Damaged potassium feldspar grains on the periphery of a deformation band, with barite cement.

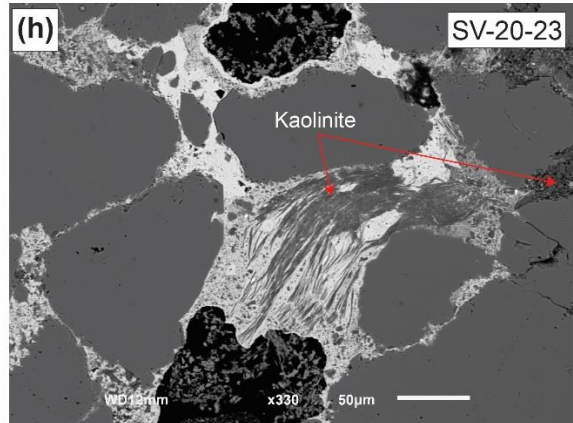
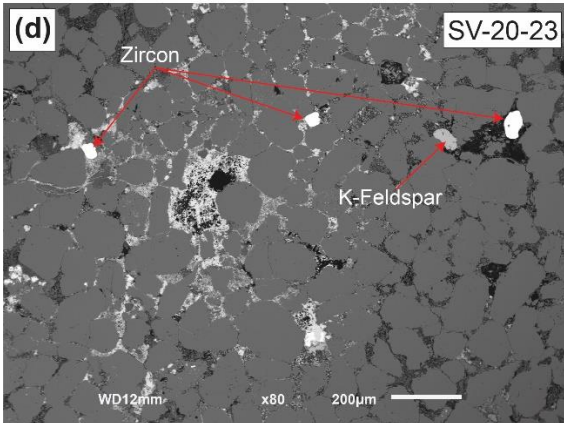
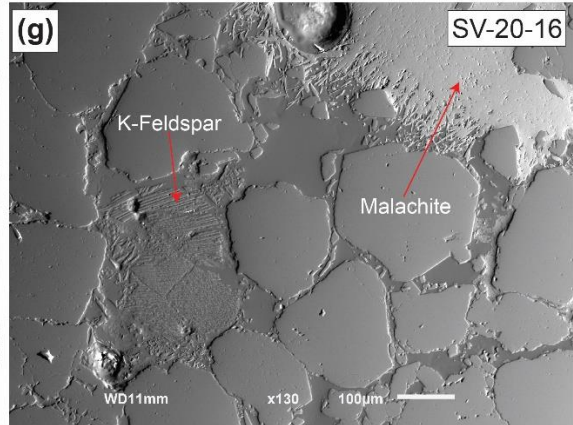
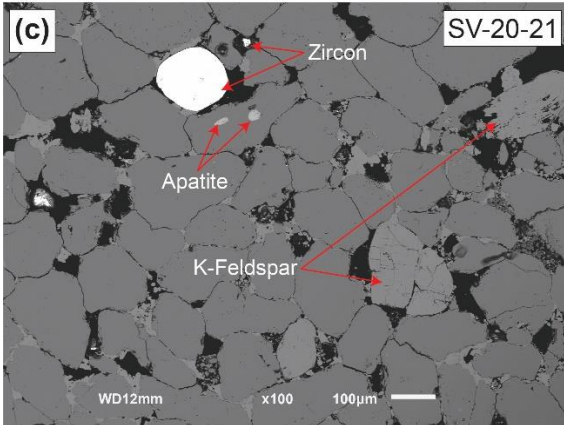
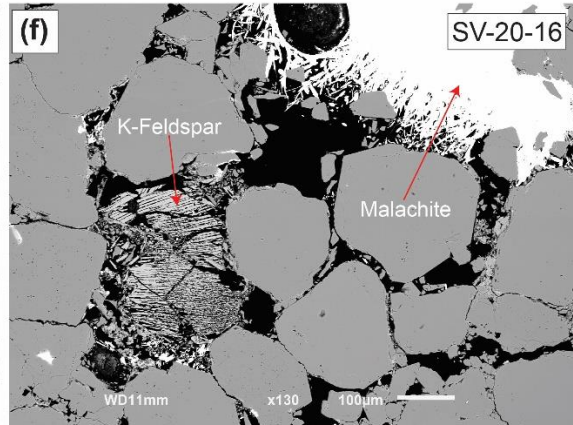
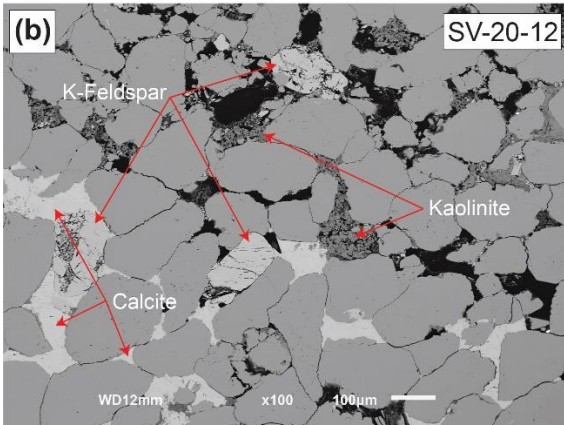
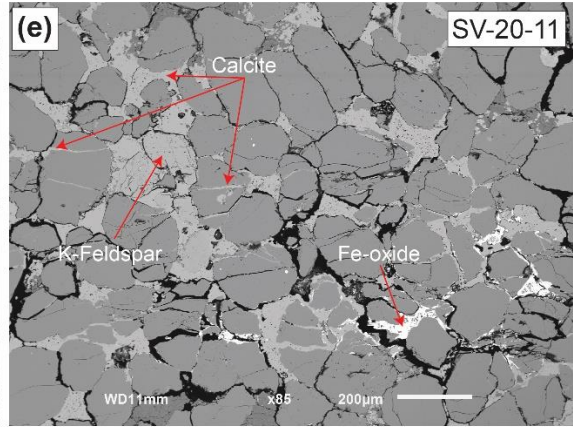
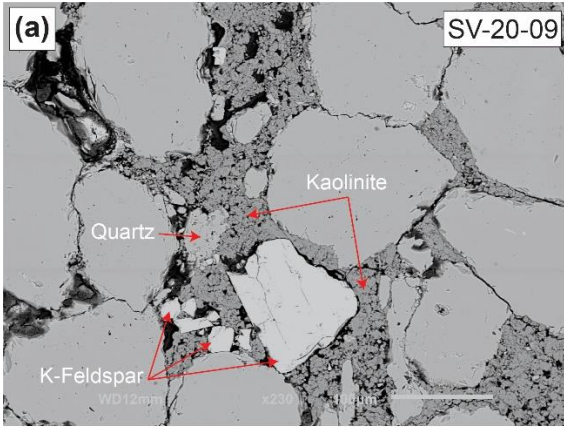


Figure 18. SEM photos collected using backscatter electron detection. Minerals were identified using X-ray spectroscopy (EDS). (a, b, c, and d) Compaction within the general matrix of samples that contain compactional deformation bands, with damaged quartz, potassium feldspar, and undamaged calcite, kaolinite, apatite, and iron oxides. (c and d) include detrital zircons and (d) has a cement composed of a mix of calcite, kaolinite, and iron oxides. (e) Shows calcite cement filling fractures in quartz grains. (f and g) are from the same location but are shown in BED-C and BED-T, respectively. (f) Malachite cement is found within fractures in sample SV-20-16 and show an incredibly damaged potassium feldspar grain. (g) Shows the different textures in quartz, potassium feldspar (highly damaged) and malachite. (h) Zooms in to sample SV-20-23 (d) just above the visible extent of the photo.

5. DISCUSSION

5.1 Structural petrology of deformation band damage zones in Salt Valley

Microstructural analysis of 26 samples from the Salt Valley indicates that within deformation bands, only detrital grains such as quartz and feldspar had experienced porosity collapse and grain cataclasis. In those same 26 samples from multiple localities surrounding the Salt Valley, none showed evidence that cement phases such as calcite or Fe-oxide were deformed in this manner. Deformation within samples typically manifests as grain fracturing, grain rotation, grain crushing, cataclastic flow, and minor pressure solution (Fig. 16) and if any of cement phases were present during deformation band formation, it is expected that they would be deformed within these band damage zones, similar to the deformation observed in detrital grains such as quartz and feldspar. In these damage zones, porosity collapse and grain cataclasis lead to significantly reduced porosity and, in turn, permeability of these units. The combined lack of observed brittle deformation of cements and the pervasive absence of cement phases within most of the deformation band examined in this study, leads us to interpret that fluid phases driving cementation arrived after the bands were formed, and thus they were not able to infiltrate these band damage zones. In the deformation bands, the only cement phases appear as late fracture fills that are undamaged (Fig. 17d and 18e). This simple observation is critical for understanding the mechanics and stress conditions under which these bands may have formed and suggests that the deformation bands likely formed when this unit was either completely uncemented or at least poorly cemented.

The interpretation that deformation banding occurred prior to the onset of pervasive cementation in these units is also supported by studies that examine the temperatures of cement formation. Bergman et al. (2013) used clumped isotope thermometry of calcite cements in sandstones near the Moab fault to determine that multiple generations of calcite growth occurred over a temperature range of 13-128°C, however the sequence of cementation phases was not clearly constrained. Later, Hodson et al. (2016) proposed that deformation bands surrounding the Moab fault zone formed before the rocks were cemented, and thus their ability to baffle fluid flow played a critical role in distributing and compartmentalizing migrating fluids that drive cementation. Using clumped isotope thermometry, that study proposed two phases of calcite cementation for the Moab member, including an earlier high-T phase (40-80° C) and a later lower-T (0-19° C) phase. By integrating this temperature data into burial history models for the region developed by Garden et al. (2001), Hodson et al. (2016) interpreted the high-T cementation phase to have occurred from 50-30 Ma, and the more recent low-T phase of cementation to have occurred within the last ~10 Myr. Like the deformation bands studied by Hodson et al. (2016) and Bergman et al. (2013), the deformation bands at Salt Valley likely formed before significant cementation of the Moab member sandstones, and thus likely indicate that early deformation in these units occurred as critical-state deformation.

5.2 Plastic strain gradients near fault planes and salt walls

The structural mapping transects presented above clearly demonstrate the presence of at least two plastic strain gradients that transect the Moab pavements; a longer wavelength gradient with length scales of ~1-3 km that diminishes away from the salt wall and/or the anticlinal axis and a short wavelength gradient that is recognized to intensify within 1-50 m of mapped and inferred brittle normal faults (Fig. 19). Additionally, a third zone of intense compactional deformation banding is recognized immediately adjacent to the salt wall.

Porous sandstones immediately adjacent to the paleo-salt wall preserve incredibly dense zones of plastic deformation. These damage zones yield deformation band accumulations of 160-186 (mm)_D/m, which is one order of magnitude higher than

deformation band accumulation rates for fault-related deformation band populations. Multiple studies have interpreted the short wavelength deformation band gradients as fault-related “damage” zones caused by motion on the adjacent faults (Antonellini and Aydin, 1995; Knott et al., 1996; Shipton and Cowie, 2001, 2003; Schueller et al., 2013; Qu et al., 2017). However, interpreting these deformation bands zones as fault-related damage requires that the fault slip itself actually drives deformation band formation. This is fundamentally problematic, as faulting results from failure of a material whilst deformation band formation results from plastic yielding, and these two rheologically-distinct deformation mechanisms are not commonly expected to be contemporaneous in a deforming material. Additionally, SEM and petrographic data presented here highlight the absence of cement in any of the deformation bands within these zones, which is here interpreted to indicate that deformation band formation must predate pervasive cementation. If matrix cements were present at the time of band formation, it should be expected that the cements themselves would also experience the comminution recognized in the matrix clasts. If correct, this should indicate that these units likely behaved as critical-state materials early in their evolution, rather than behaving as Mohr-Coulomb materials, as would be required for faulting.

Despite the finding of this study that show that deformation bands are unlikely to represent fault damage zones, it is clear that many of the deformation bands in this region are related to faulting in some way. Previous studies have also shown that deformation bands are typically abundant near fault surfaces, with an exponential decrease in deformation band abundance as distance from fault planes increase (Schueller et al., 2013; Johansen and Fossen, 2008). Significant spikes in cumulative deformation band thickness along the long wavelength gradient are associated with faulting (e.g., the faults identified on Fig. 19). Our dataset is limited to traverses across 7 mapped faults (Figs. 9 & 11) however, faults with more displacement are associated with larger zones of deformation bands and a higher overall rate of deformation band accumulation. Of those mapped, Transect #13 has the two faults (A and B, see Fig. 19) with the most fault throw; these faults also have the highest overall deformation band accumulation rates. Fault A accumulated 57 cm of deformation band thickness over a lateral distance of 31 m, and fault B accumulated 70 cm of deformation band thickness over a later distance of 48 m,

thus the highest rates of deformation band thickness accumulation are found in the damage zones associated with faults A and B, with both faults A and B having an overall deformation band accumulation rate of 14.4 (mm)_D/m. Deformation band accumulation rates do not vary significantly with varying fault throw and deformation band distributions, with faults C and D (Fig. 19) showing the lowest accumulation rates of 10.4 (mm)_D/m and 10.8 (mm)_D/m, respectively. Importantly, deformation band accumulation rates are not dependent on distance from paleo-salt walls. The fault related deformation band distributions appear to be related to fault throw, with larger displacement faults having larger populations of deformation bands and higher deformation band accumulation rates. These observations are similar to observations from Schueller et al. (2013) where larger displacement faults tend to have more deformation bands per meter over longer distances.

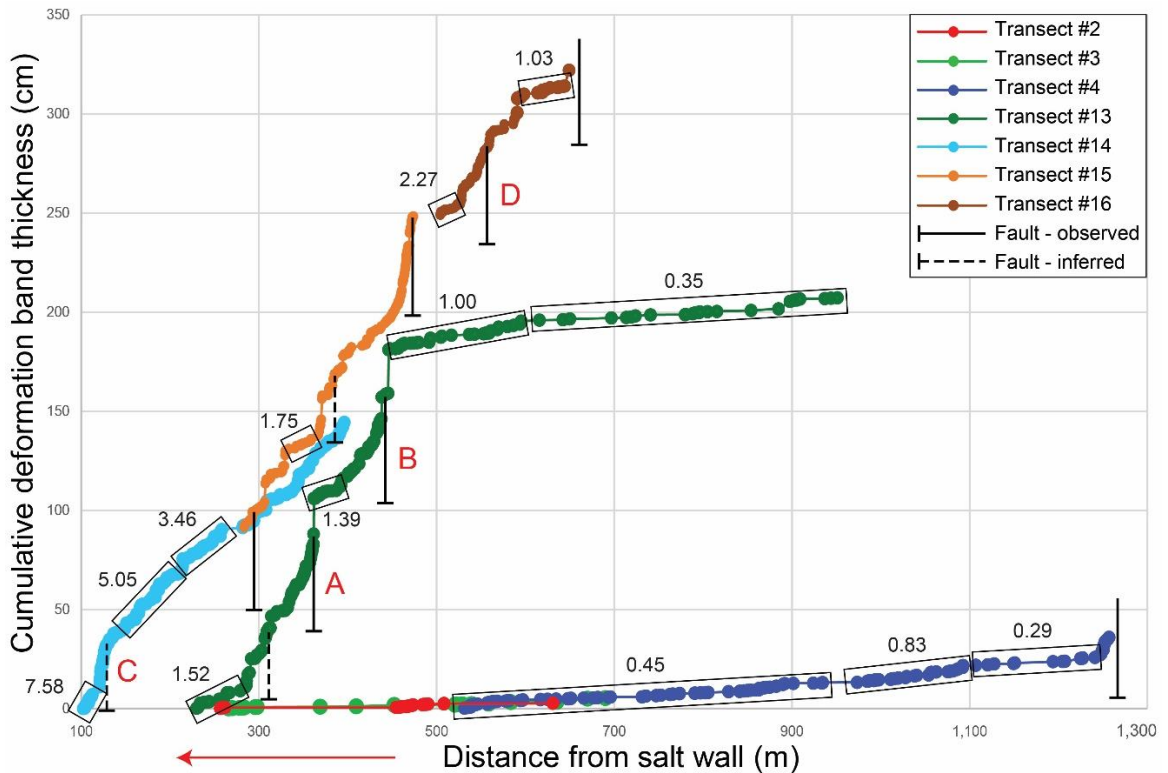


Figure 19. Compiled cumulative thickness plots with calculated slope values for the accumulation segments of the line (black boxes) that represent the long wavelength gradient that decreases with distance to the Salt Valley salt wall. Fault locations are marked with a black line (solid when observed and dashed when inferred). The Fiery Furnace and Delicate Arch transects are located on the northeastern limb of the Salt Valley anticline and the Valley City transects are on the

southwest limb of the anticline. Notice that even though the slope gradients are similar, the cumulative thicknesses on the northeastern limb are approximately one order of magnitude greater than the southwestern limb.

In the long wavelength strain gradient, deformation bands are pervasive and can be found up to ~2,800 meters from the interpreted paleo-salt wall boundaries. Deformation band accumulation rates of 7.58 (mm)_D/m are recorded within ~100 meters of salt wall contacts, indicating significant strain accommodation in high porosity sandstones within ~100 meters of the salt bodies. These long wavelength gradients then diminish away from the salt wall and/or the anticlinal axis of the Salt Valley, however the rate of diminishment varies along the length of valley. For example, Transects #14, #15 and #16 would have experienced the highest finite plastic strain, with ~250 cm of cumulative deformation band thickness over a lateral distance of ~650 m, and an overall accumulation rate of 3.85 (mm)_D/m. Transect #13 experienced slightly less strain, with ~205 cm of deformation band thickness over a distance of ~750 m, (overall accumulation rate of 2.73 (mm)_D/m). While Transect #4 would have experienced much lower strain, with ~40 cm of deformation band thickness over a distance of ~1,250 m (overall accumulation rate of 0.32 (mm)_D/m). At the longest lateral distance from the salt wall and approaching the synclinal axis between the Salt and Moab Valleys, deformation banding is almost completely absent. Although it remains unclear whether or not this long wavelength gradient is produced by pressure created by the rising salt and/or anticlinal doming of the Jurassic salt, we propose possible mechanisms of formation based on comparison with numerical models in the following section.

5.3 Comparison of results with numerical models of diapir formation

Thigpen et al. (2019) used forward finite element modeling of salt system evolution to understand the evolution of salt diapirs and their surrounding wall and cover sequences in the downdip extensional (compressional) domain of a gravity driven passive margin system (Fig. 20). In these models, the downdip flow of salt into the compressional toe of the system leads to salt inflation and doming of the cover sequences, active diapirism and salt tunneling of the most downdip diapir, and eventually reactive diapirism to form a second major diapir updip of the first one (Fig. 21). During this

evolution, the numerical model predicts multiple zones of strain development. First, during the early stages of salt inflation, formation of the salt cored anticline drives the overburden cover sequence into extension (Fig. 22). In this phase, the model predicts the development of outer-arc extension, which is manifested as initially diffuse but pervasive extension followed by progressive localization to normal faulting. In the Salt Valley system, diffuse extensional strain is manifested as the steeply dipping deformation bands that commonly preserve evidence for normal-sense shearing. Additionally, normal faults, including those surrounded by dense deformation band zones, are common. The similarities between the model predictions and the observations in the Salt Valley system lead us to provisionally interpret that doming of the overburden due to salt rise may be the cause of both the diffuse and discretized extensional deformation in this system. However, modeled extension and doming does not predict the high degree of deformation observed immediately adjacent to the salt wall and in the overlying roof pendants. Additionally, the model predicts a progression from diffuse deformation transitioning to discretized normal faulting, which contrasts with the idea that these normal faults produce diffuse “damage” zones.

In regards to the former, the model also predicts that the salt diapir is capable of essentially tunneling through the overburden as it goes into extension, and this produces a pronounced strain gradient immediately adjacent to the rising diapir (Fig. 23). Finite plastic strain values in the model indicate that a diapir ~ 1 km in width creates a plastic strain gradient in the adjacent cover and wall rocks, with finite plastic strains values of >250% within 100-300 meters of the salt wall and >50% ~3 km distance from the diapir (Fig. 23). Because of this, we propose that such a tunneling effect may explain the strain patterns observed in the wall rocks and roof pendants directly adjacent to the salt. If correct, the model predictions can match the observation of the development (and potentially overprinting) of two spatially and distinct zones of extension and compression, respectively, in the same system. However, it should be noted that this model requires an active diapiric mechanism rather than a traditionally passive mechanism that has been proposed by multiple studies.

In regards to the latter, as mentioned previously, the implicit mechanics of the fault “damage” zone hypothesis remain problematic. Essentially, plastic yielding and

Mohr-Coulomb failure are rheologically distinct mechanisms, and thus it is difficult to envision a process wherein brittle failure of “strong” rock leads to diffuse plastic yielding in the surrounding material. However, this progression can be reversed. The creation of dense zones of deformation bands is basically a strain hardening process, wherein progressive plastic yielding leads to strengthening of the material. Here, we propose that deformation bands can strain harden an area large enough for a brittle fault to form contemporaneously with, albeit following, the formation of deformation bands. If correct, this could account for suitable comparisons between the structures observed in the Salt Valley and those predicted by the numerical model, with the caveat that these normal faults and deformation bands are essentially contemporaneous. Thus, we also propose that the normal faults proximal to the Salt Valley salt wall are early structural features associated with extension that eventually allowed for vertical growth of the Salt Valley salt diapir. It is important to note that there is also a less numerous set of normal faults that were active much later in the evolution of this system, as erosion and salt dissolution caused roof collapse and small displacement normal faults to form on the eroding margins of the Salt Valley.

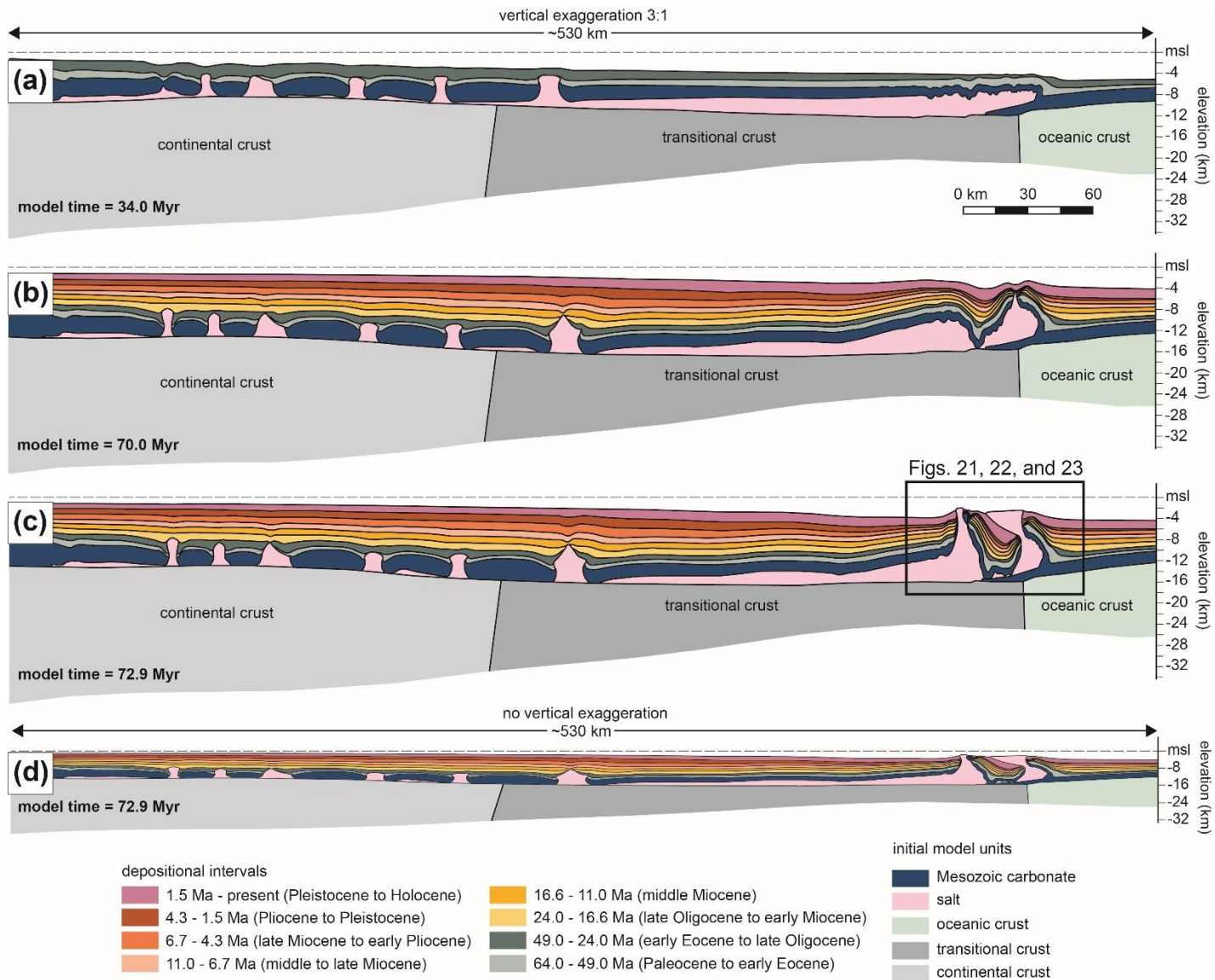


Figure 20. Finite element model results for RS2 model produced by Thigpen et al. (2019). (a) A linked extensional and contractional gravity driven system with extension in the upgradient section, and an autochthonous salt layer in the downgradient section. (b) Basinward progradation of the sediment wedge drives basinward salt flow, which causes two salt domes to form anticlines and an incipient salt diapir as salt begins to pierce overburden material. (c) Two salt diapirs develop, causing intense short wavelength folding and rotation of beds as the salt “tunneled” to the surface. (d) Model results shown with no vertical exaggeration.

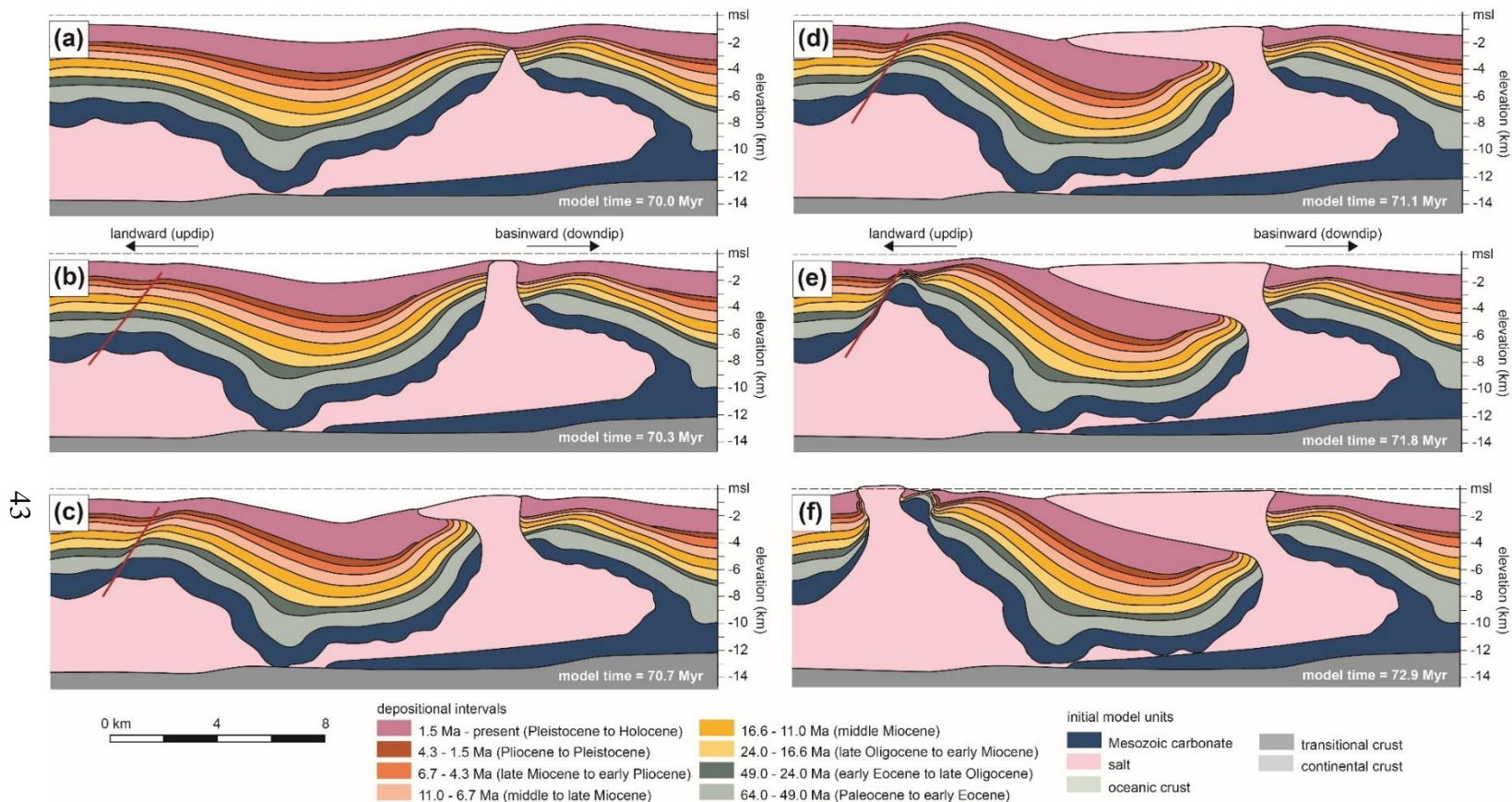
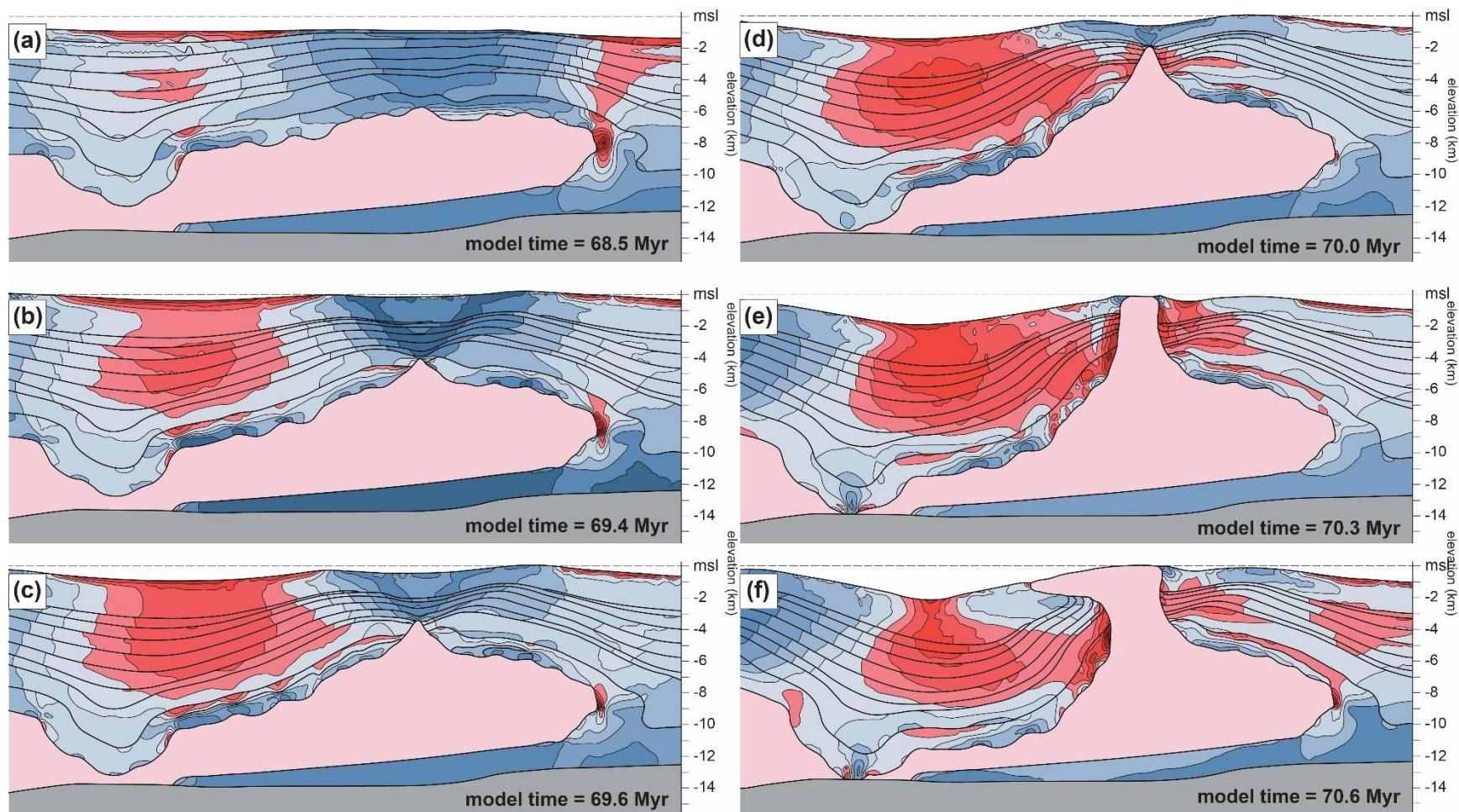


Figure 21. Evolution of the downdip contractional section in the RS2 model. (a) The cover sequence above the downdip anticline extends and thins and salt begins to pierce overburden material. (b) The downdip diapir continues to grow as salt flows vertically and nearly pierces the surface/water interface. Clockwise rotation of the middle limb begins and a fault forms above the updip diapir. (c) Continued clockwise rotation of the common limb drives further growth of the downdip diapir, as deformation, in the form of folding and plastic strain is pervasive in folded wall rocks. (d–f) Salt welds have cutoff the salt supply and minor growth of the downdip diapir continues as the common limb collapses and mobilizes the remaining available salt. Concurrently, salt in the updip diapir takes advantage of the fault and a second diapir emerges, causing intense folding in wall rocks.



0 m 2000 4000 6000

horizontal stress / vertical stress ratio (K_0)

0.5 0.6 0.7 0.8 0.9 1.0 1.1 1.2 1.3 1.4 1.5 1.6 1.7

extensional isotropic contractural

salt

Figure 22. (a) An extensional stress field is created during the onset of outer arc extension (b) Progressive development of nascent crestal normal faults associated with outer arc extension that initiated and focused vertical salt flow. (c) As vertical salt flow continues, wall rocks on the flanks of the emerging diapir transition from extensional to near isotropic, with lesser extension present at the tip of the salt. (d) Further diapir growth causes a transition in the wall rocks from isotropic to compressional, while overburden near the tip of the emerging diapir remains in extension. (e) The salt diapir has nearly reached the surface and compression of wall rocks create contractional strain in wall rocks. (f) Further diapir growth caused deformation, in the form of folding and plastic strain

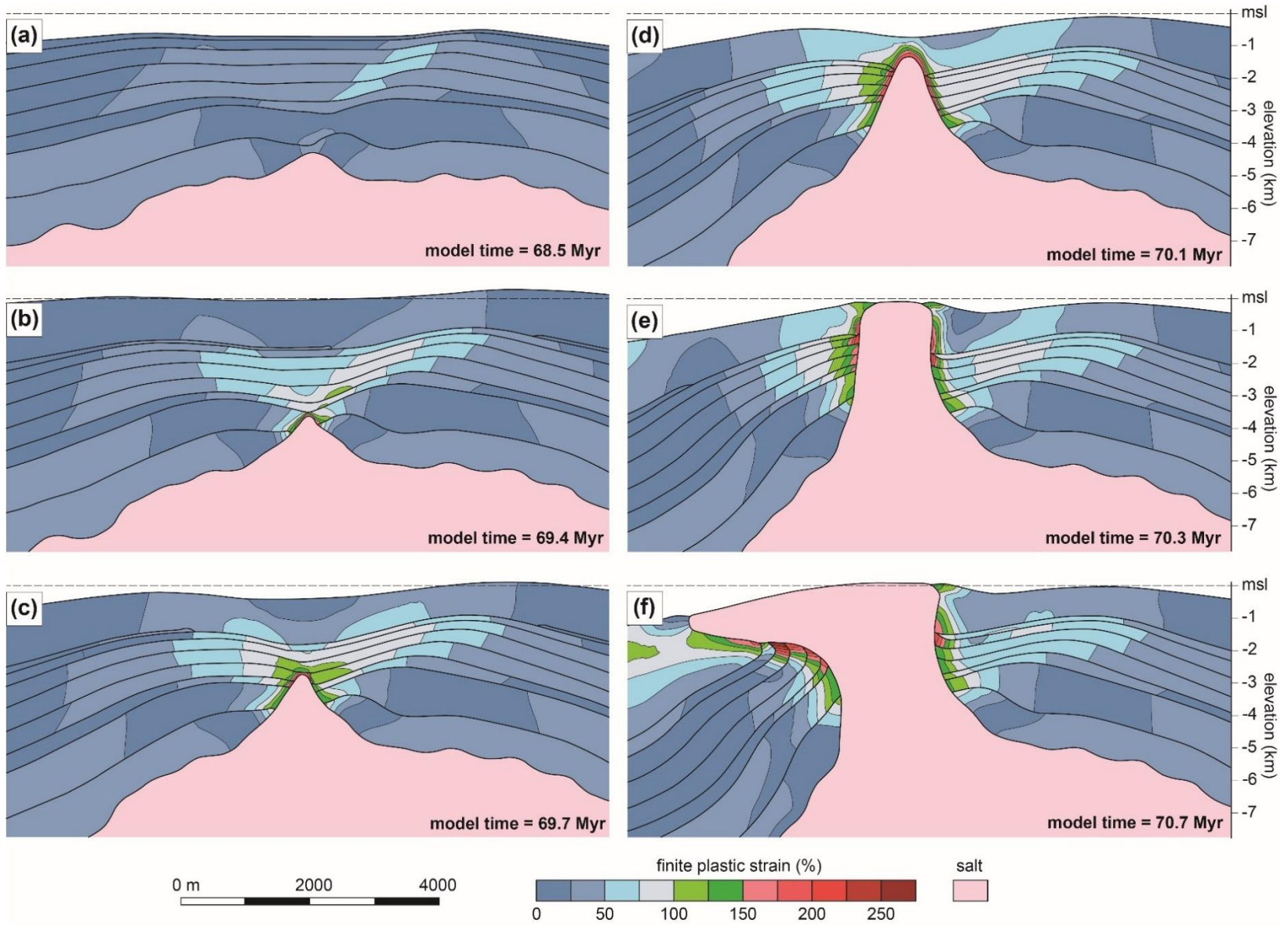
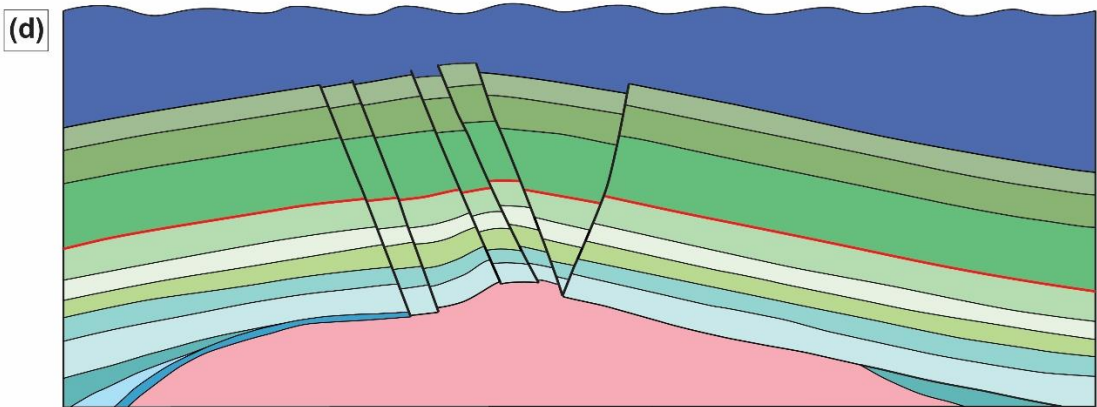
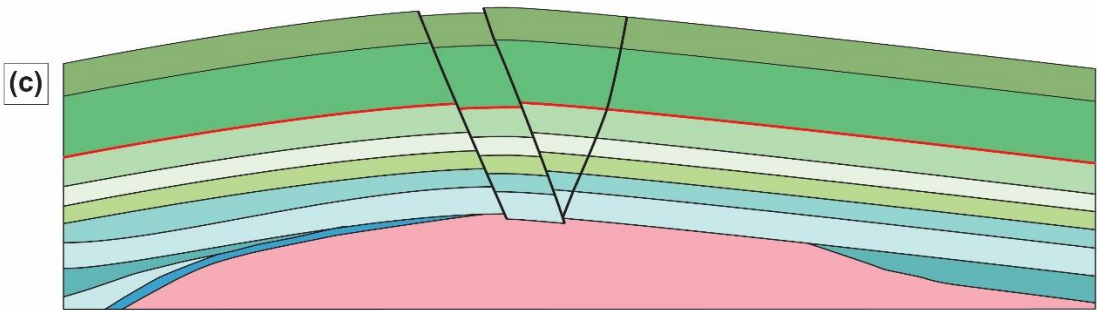
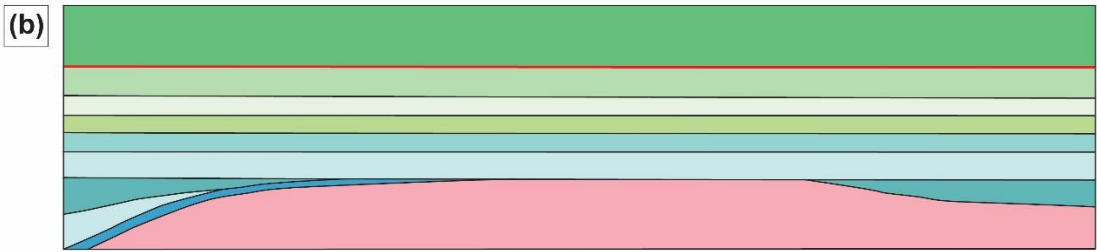
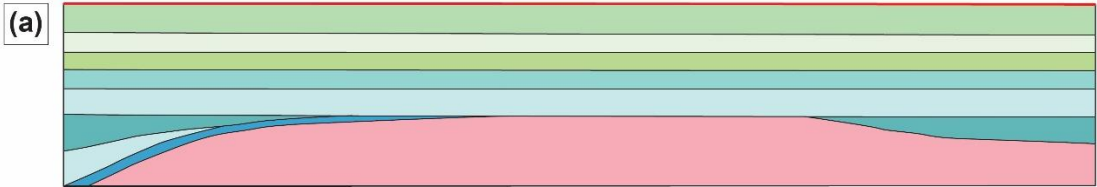
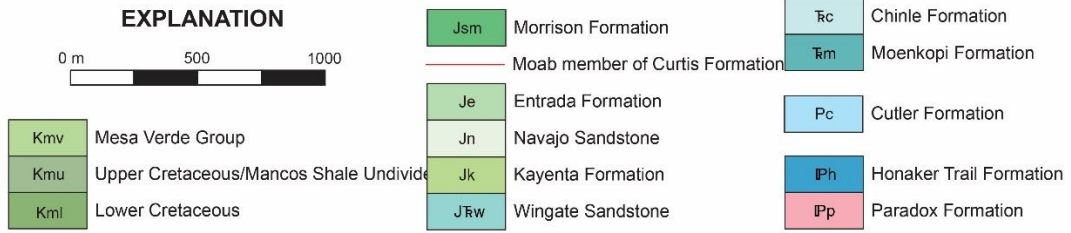


Figure 23. (a) An extensional field develops over the doming salt. (b-c) Diapirism is initiated as salt begins to pierce overburden material. During this time, the overburden is in extension, but there is compressional plastic strain at the front of the emerging salt diapir. (d-e) Plastic compressional strain increases on wall rocks as the diapir grows vertically to just beneath the sediment/water interface. (f) As salt emerges and begins to form a canopy, plastic strain localized in high porosity units as mobile salt folds and overturns wall rocks.



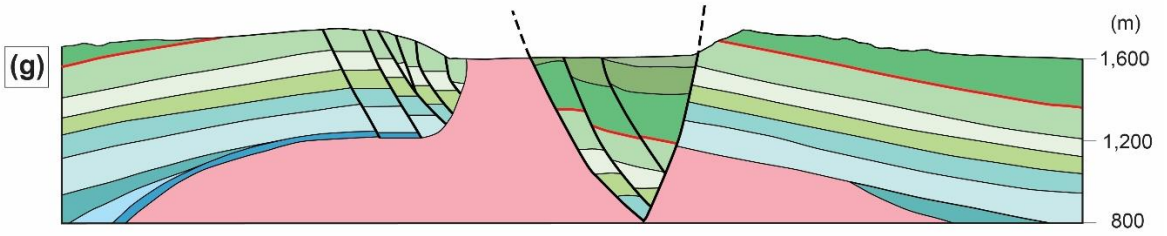
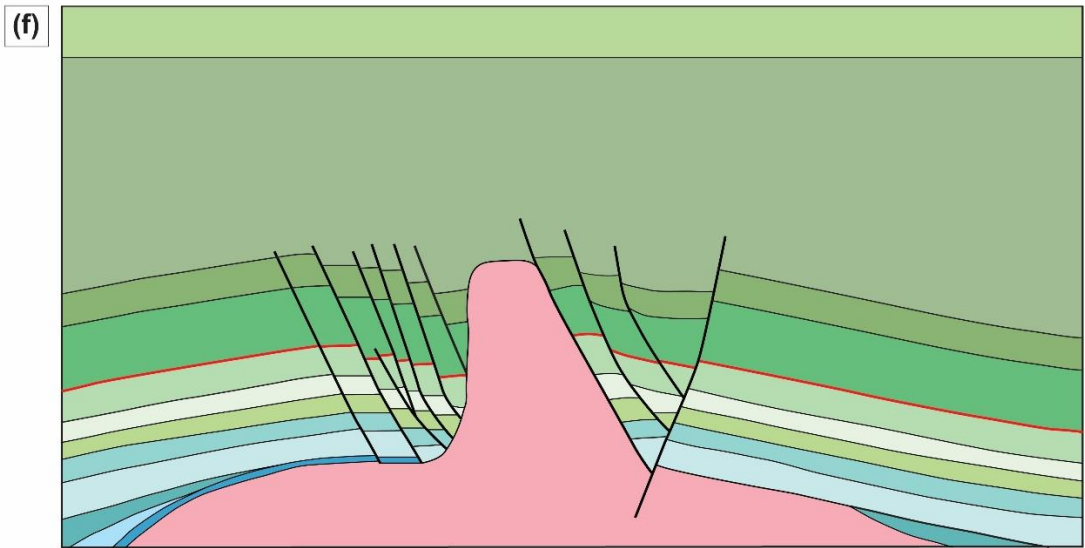
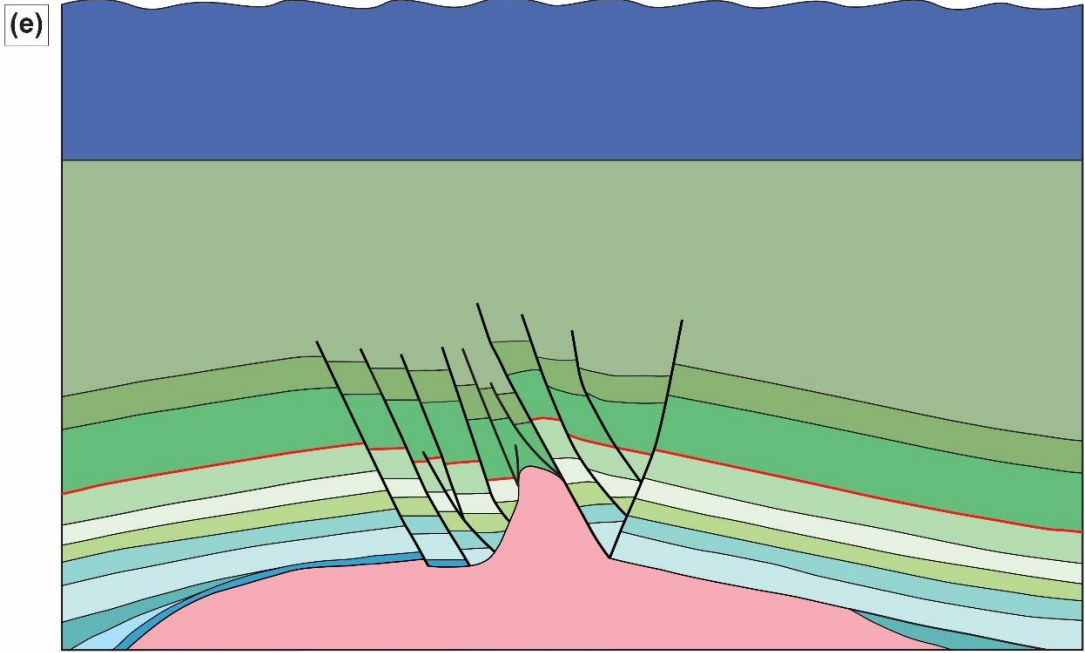


Figure 24. Structural evolution of northern Salt Valley (cross section location labeled as A-A' in Fig. 7). (a) Represent the general stratigraphy after deposition of the Moab member, with unit thicknesses derived from Doelling, 2001. After diapirism ceased in the late Triassic, deposition of largely aeolian sandstones throughout most of the Jurassic. (b) Stratigraphy after deposition of the Morrison Formation. (c) Stratigraphy after deposition of the early Cretaceous units. Differential loading causes an extensional stress field to form in Jurassic and early Cretaceous overburden, and outer arc extension causes deformation bands and normal faults. (d) Stratigraphy after formation of the Cretaceous seaway and deposition of ~100 meters of Mancos Shale. Overburden continues to fault as salt begins to rise into space created by crestal extension. (e) After deposition of the Mancos Shale and before the Cretaceous seaway retreated. Salt is actively tunneling through overburden, which is displaced laterally. (f) Final geometry after diapir growth stops. (g) Cross section of modern northern Salt Valley. Location of cross section line is shown in Figure 7. An elevation profile was created using ArcMap and it was fit to the modern geology (modified after Jackson and Hudec, 2017) Erosion has formed the modern Salt Valley, with normal faulted blocks in the valley floor that have traveled up to ~500 meters.

6. CONCLUSIONS

In the Salt Valley, UT, mesoscale structural mapping normal to the paleo-salt walls reveals two plastic strain gradients represented by deformation banding. A long wavelength plastic strain gradient composed of steeply dipping ($60\text{-}75^\circ$) normal-sense deformation or shear bands extends 1-3 km away from paleo-salt wall contacts, with average band densities of 7.6 (mm)^D/m near paleo-salt walls, ~1.0 (mm)^D/m at distances of 500 meters, and dissipating to no visible deformation bands at 1,500-2,800 meters. A short wavelength (1-50 m) plastic strain gradient was also recognized in the vicinity of meso- to map-scale brittle normal faults, wherein deformation bands dissipated in number and intensity extending away from fault planes. Plots of accumulated deformation band thickness indicate that distributed deformation bands along the long wavelength gradient decrease in number and intensity with increasing distance from either the paleo-salt wall or the anticlinal axis, whereas the distribution of deformation bands associated with the short wavelength gradient shows a clear positive correlation between deformation band thickness accumulations and the magnitude of throw of the brittle normal faults. Lastly, a third zone of intense compactional deformation banding is recognized immediately adjacent to the interpreted paleo-salt wall or in “roof pendants” that presumably sat on top of the salt dome and are now preserved in the valley floor.

Petrographic and SEM analysis of 26 deformation band samples show that bands are primarily composed of cataclastically fractured detrital quartz and feldspar grains.

Importantly, cement phases that include calcite, barite, Fe-oxide, Ti-oxide, and malachite are never observed to be deformed within deformation bands, leading us to interpret that the cements post-date these features. Commonly, these cements that are pervasive in the host-rock matrix are observed filling late fractures in quartz grains and deformation bands. This observation also leads us to interpret that the deformation bands preserved on the limbs of the Salt Valley anticline formed as a plastic critical state yielding response, as opposed to traditional Mohr-Coulomb failure behavior commonly applied to rocks. Although the plastic yielding and brittle failure mechanisms are rheologically distinct, the similar orientation, slip sense, and clear relationship between the fault-related bands and the brittle fault planes leads us to further interpret that when deformation bands progressively form dense zones, this may lead to strain hardening that eventually progresses to brittle (Mohr-Coulomb) failure.

Based on comparison with the results of forward numerical models, we interpret that the long wavelength deformation band gradient likely formed during outer arc extension of the overburden (including the Moab member) during doming of the salt anticline. In this scenario, pervasive and distributed extension is accommodated by these normal sense deformation/shear bands, with some progressing to form dense clusters that eventually strain harden the material and commence failure as normal faults. The latter would explain the short wavelength gradients that are observed near faults. Finally, the models predict that salt tunneling through overburden material, contemporaneous with doming, should drive development of intense zones of compactional deformation, such as those observed near the paleo-salt wall. This type of model holistically explains the observations from Salt Valley, and can account for the simultaneous development of the extensional (long wavelength) deformation banding, the normal faults with associated short wavelength band “damage” zones, and the compactional zones observed immediately adjacent to salt and within the roof pendants. This revised mechanistic understanding of deformation band formation during salt evolution may allow us to better predict such damage zones in high-porosity units, such as oil reservoirs, even in the absence of data such as cores.

REFERENCES

- Antonellini, M.A., and Aydin, A., 1995. Effect of faulting on fluid flow in porous sandstone: Geometry and spatial distribution. *AAPG Bulletin* 79, 642-671, doi.org/10.1306/8D2B1B60-171E-11D7-8645000102C1865D.
- Antonellini, M.A., Aydin, A., and Pollard, D.D., 1994. Microstructure of deformation bands in porous sandstones at Arches National Park, Utah. *Journal of Structural Geology* 16, 941-959, doi.org/10.1016/0191-8141(94)90077-9.
- Aydin, A., and Johnson, A.M., 1978. Development of faults as zones of deformation bands and as slip surfaces in sandstone. *Pure and Applied Geophysics* 116, 931-942, doi.org/10.1007/BF00876547.
- Aydin, A., Borja, R.I., and Eichhubl, P., 2006. Geological and mathematical framework for failure modes in granular rock. *Journal of Structural Geology* 28, 83–98, doi.org/10.1016/j.jsg.2005.07.008.
- Baars, D.L., 1966. Pre-Pennsylvanian paleotectonics – key to basin evolution and petroleum occurrences in Paradox Basin, Utah and Colorado. *AAPG Bulletin*, 50, 2082-2111, doi.org/10.1306/5D25B70D-16C1-11D7-8645000102C1865D.
- Baars, D.L., and Stevenson, G.M., 1981. Tectonic evolution of the Paradox Basin, Utah & Colorado. *Rocky Mountain Association of Geologists, 1981 Field Conference*, 23-31.
- Ballas, G., Fossen, H., and Soliva, R., 2015. Factors controlling permeability of cataclastic deformation bands and faults in porous sandstone reservoirs. *Journal of Structural Geology*, 76, 1-21, doi.org/10.1016/j.jsg.2015.03.013.
- Berg, S.S., and Skar, T., 2005. Controls on damage zone asymmetry of a normal fault zone: outcrop analyses of a segment of the Moab fault, SE Utah. *Journal of Structural Geology*, 27, 1803-1822, doi.org/10.1016/j.jsg.2005.04.012.
- Bergman, S.C., Huntington, K.W., and Crider, J.G., 2013. Tracing paleofluid sources using clumped isotope thermometry of diagenetic cements along the Moab Fault, Utah. *American Journal of Science*, 313, 490-515, doi.org/10.2475/05.2013.03.
- Blakey, R.C., 2014. Paleogeography and Paleotectonics of the Western Interior Seaway, Jurassic-Cretaceous of North America. *Search and Discovery*, 30392, 72.
- Crawford, B.R., 1998. Experimental fault sealing: shear band permeability dependency on cataclastic fault gouge characteristics. In: Coward, M.P., Daltaban, T.S., Johnson, H. (Eds.), *Structural Geology in Reservoir Characterization*, Geological Society of London Special Publication, 127, 27– 47, doi.org/10.1144/GSL.SP.1998.127.01.04.
- Crook, A.J.L., Owen, D.R.J, Willson, S.M., and Yu, J.G, 2006. Benchmarks for the evolution of shear localisation with large relative sliding in frictional materials. *Computer*

Methods in Applied Mechanics and Engineering, 195, 4991-5010,
doi.org/10.1016/j.cma.2005.11.016.

Davis, D.M., and Engelder, T., 1985. The role of salt in fold-and-thrust-belts.
Tectonophysics, v. 119, 67-88, doi.org/10.1016/0040-1951(85)90033-2.

Doelling, H.H., Oviatt, C.G., and Huntoon, P.W., 1988. Salt deformation in the Paradox region. Utah Geological and Mineral Survey, 122, 93.

Doelling, H.H., 2001. Geologic map of the Moab and eastern part of the San Rafael Desert 30' X 60' Quadrangles, Grand and Emery Counties, Utah, and Mesa County, Colorado. Utah Geological Survey.

Doelling, H.H., and Kuehne, P.A., 2013. Geologic Maps of the Klondike Bluffs, Mollie Hogans, and The Windows Section 7.5' Quadrangles, Grand County, Utah. Utah Geological Survey, Map 258DM, Map 259DM, and Map 260DM, 1-31.

Fiduk, J.C., Weimer, P., Trudgill, B.D., Rowan, M.G., Gale, P.E., Phair, R.L., Korn, B.E., Roberts, G.R., Gafford, W.T., Lowe, R.S., and Queffelec, T.A., 1999. The Perdido Fold Belt, Northwestern Deep Gulf of Mexico, Part 2: Seismic Stratigraphy and Petroleum Systems 1. AAPG Bulletin, 83, 578-612, doi.org/10.1306/00AA9C00-1730-11D7-8645000102C1865D.

Fossen, H., 2010. Deformation bands formed during soft-sediment deformation: Observations from SE Utah. Marine and Petroleum Geology, 27, 215-222, doi.org/10.1016/j.marpetgeo.2009.06.005.

Fossen, H., and Hesthammer, J., 1997. Geometric analysis and scaling relations of deformation bands in porous sandstone: Journal of Structural Geology, 19, 1479-1493, doi.org/10.1016/S0191-8141(97)00075-8.

Fossen, H., Schultz, R.A., Shipton, Z.K., and Mair, K., 2007. Deformation bands in sandstone: a review. Journal of the Geological Society, London, 164, 755-769, doi.org/10.1144/0016-76492006-036.

Fossen, H., Schultz, R.A., and Torabi, A., 2011. Conditions and implications for compaction band formation in the Navajo Sandstone, Utah. Journal of Structural Geology, 33, 1477-1490, doi.org/10.1016/j.jsg.2011.08.001.

Garden, J.R., Guscott, S.C., Burley, S.D., Foxford, K.A., Walsh, J.J., and Marshall, J., 2001. An exhumed palaeo-hydrocarbon migration fairway in a faulted carrier system, Entrada Sandstone of SE Utah, USA. Geofluids, 1, 195-213, doi.org/10.1046/j.1468-8123.2001.00018.x.

Hodson, K.R., Crider, J.G., and Huntington, K.W., 2016. Temperature and composition of carbonate cements record early structural control on cementation in a nascent

deformation band fault zone: Moab Fault, Utah, USA. *Tectonophysics*, 690, 240-252, doi.org/10.1016/j.tecto.2016.04.032.

Hudec, M.R., and Jackson, M.P.A., 2007. Terra infirma: Understanding salt tectonics. *Earth Science Review*, 82, 1-28, doi.org/10.1016/j.earscirev.2007.01.001.

Jackson, M.P.A., and Hudec, M.R., 2017. *Salt tectonics: principles and practice*. Cambridge University Press, 498, doi.org/10.1017/9781139003988.

Johansen, T.E.S., and Fossen, H., 2008. Internal geometry of fault damage zones in interbedded siliciclastic sediments. *The Geological Society of London*, 299, 35-56, doi.org/10.1144/SP299.3.

Knott, S.D., Beach, A., Brocknank, P.J., Brown, J.L., McCallum, J.E., and Welbon, A.I., 1996. Spatial and mechanical controls on normal fault populations. *Journal of Structural Geology*, 18, 359-372, https://doi.org/10.1016/S0191-8141(96)80056-3.

Kolyukhin, D., Schueller, S., Espedal, M.S., and Fossen, H., 2010. Deformation band populations in fault damage zone – impact on fluid flow. *Computer and Geosciences*, 14, 231-248, dx.doi.org/10.1007/s10596-009-9148-8.

Lawton, T.F., Buller, C.D., and Parr, T.R., 2015. Provenance of a Permian erg on the western margin of Pangea: Depositional system of the Kungurian (late Leonardian) Castle Valley and White Rim sandstones and subjacent Cutler Group, Paradox Basin, Utah, USA. *Geosphere*, 11, 1475-1506, doi.org/10.1130/GES01174.1.

Lawton, T.F., Vega, F.J., Giles, K.A., and C. Rosales-Domínguez, 2001. Stratigraphy and origin of the La Popa Basin, Nuevo León and Coahuila, Mexico, in C. Bartolini, R.T. Buffler, and A. Cantú-Chapa, eds., *The western Gulf of Mexico Basin: Tectonics, sedimentary basins, and petroleum systems: AAPG Memoir 75*, 219-240.

Mair, K., Main, I., and Elphick, S., 2000. Sequential growth of deformation bands in the laboratory. *Journal of Structural Geology* 22, 25-42, doi.org/10.1016/S0191-8141(99)00124-8.

Mair, K., Elphick, S., and Main, I., 2002. Influence of confining pressure on the mechanical and structural evolution of laboratory deformation bands. *Geophysical Research Letters*, 29, no. 10, doi.org/10.1029/2001GL013964.

Nikolinakou, M.A., Heidari, M., Hudec, M.R., and Flemings, P.B., 2017. Initiation and growth of salt diapirs in tectonically stable settings: Upbuilding and megaflaps. *AAPG Bulletin*, 101, 887-905, doi.org/10.1306/09021615245.

Nuccio, V.F., and Condon, S.M., 1996. Burial and Thermal History of the Paradox Basin, Utah and Colorado, and Petroleum Potential of the Middle Pennsylvanian Paradox Formation. *U.S. Geological Survey Bulletin* 2000, 39, doi.org/10.3133/b000

Okubo, C.H., and Schultz, R.A., 2007. Compactional deformation bands in Wingate Sandstone; additional evidence of an impact origin for Upheaval Dome, Utah. *Earth and Planetary Science Letters*, 256, 169-181, <https://doi.org/10.1016/j.epsl.2007.01.024>.

Ogilvie, S.R., and Glover, P.W.J., 2001. The petrophysical properties of deformation bands in relation to their microstructure. *Earth and Planetary Science Letters*, 193, 129-142, [doi.org/10.1016/S0012-821X\(01\)00492-7](https://doi.org/10.1016/S0012-821X(01)00492-7).

Qu, D., Tveranger, J., and Fachri, M., 2017. Influence of deformation-band fault damage zones on reservoir performance. *Interpretation*, 5, SP41-SP56, [dx.doi.org/10.1190/INT-2016-0229.1](https://doi.org/10.1190/INT-2016-0229.1).

Rotevatn, A., and Fossen, H., 2011. Simulating the effect of subseismic fault tails and process zones in a siliciclastic reservoir analogue: Implications for aquifer support and trap definition. *Marine and Petroleum Geology*, 28, 1648-1662, doi.org/10.1016/j.marpetgeo.2011.07.005.

Rowan, M.G., Peel, F.J., and Vendeville, B.C., 2004. Gravity-driven fold belts on passive margins. *AAPG Memoir* 82, 157-182, doi.org/10.1306/M82813C9.

Rowan, M.G., Peel, F.J., Vendeville, B.C. and Gaullier, V. 2012. Salt tectonics at passive margins: Geology versus models – Discussion: *Marine and Petroleum Geology*, v. 37, p. 184-194, <https://doi.org/10.1016/j.marpetgeo.2012.04.007>.

Schueller, S., Braathen, A., Fossen, H., and Tveranger, J., 2013. Spatial distribution of deformation bands in damage zones of extensional faults in porous sandstones: Statistical analysis of field data. *Journal of Structural Geology*, 52, 148-162, <http://dx.doi.org/10.1016/j.jsg.2013.03.013>

Schultz, R.A., and Siddharthan, R., 2005. A general framework for the occurrence and faulting of deformation bands in porous granular rocks. *Tectonophysics* 411, 1-18, doi.org/10.1016/j.tecto.2005.07.008.

Sepehr, M., and Cosgrove, J.W., 2004. Structural framework of the Zagros Fold-Thrust Belt, Iran. *Marine and Petroleum Geology*, 21, 829-843, doi.org/10.1016/j.marpetgeo.2003.07.006.

Shipton, Z.K., and Cowie, P.A., 2001. Damage zone and slip-surface evolution over μm to km scales in high-porosity Navajo sandstone, Utah. *Journal of Structural Geology*, 23, 1825-1844, [doi.org/10.1016/S0191-8141\(01\)00035-9](https://doi.org/10.1016/S0191-8141(01)00035-9).

Shipton, Z.K., and Cowie, P.A., 2003. A conceptual model for the origin of fault damage zone structures in high-porosity sandstone. *Journal of Structural Geology*, 25, 333-344, [doi.org/10.1016/S0191-8141\(02\)00037-8](https://doi.org/10.1016/S0191-8141(02)00037-8).

Shipton, Z.K., Evans, J.P., Robeson, K., Forster, C.B., and Snelgrove, S., 2002. Structural heterogeneity and permeability in faulted eolian sandstone: implications for subsurface modelling of faults. *American Association of Petroleum Geologists Bulletin* 86, 863–883, doi.org/10.1306/61EEDBC0-173E-11D7-8645000102C1865D.

Soliva, R., Ballas, G., Fossen, H., and Philit, S., 2016. Tectonic regime controls clustering of deformation bands in porous sandstone. *Geology*, Geological Society of America, 44, 423-426, doi:10.1130/G37585.1.

Solum, J.G., Brandenburg, J.P., Naruk, S.J., Kostenko, O.V., Wilkins, S.J., and Schultz, R.A., 2010. Characterization of deformation bands associated with normal and reverse stress states in the Navajo Sandstone, Utah. *AAPG Bulletin*, 94, 1453-1475, dx.doi.org/10.1306/01051009137.

Thigpen, J.R., Roberts, D., Snow, J.K., Walker, C.D., and Bere, A., 2019. Integrating kinematic restoration and forward finite element simulations to constrain the evolution of salt diapirism and overburden in evaporate basins. *Journal of Structural Geology* 118, 68-86, doi:10.1016/j.jsg.2018.10.003.

Torabi, A., and Fossen, H., 2009. Spatial variation of microstructure and petrophysical properties along deformation bands in reservoir sandstones. *AAPG Bulletin*, 93, 919-938, doi.org/10.1306/03270908161.

Vajdova, V., Baud, P., and Wong, T.f., 2004. Permeability evolution during localized deformation in Bentheim sandstone. *Journal of Geophysical Research* 109, B10406. doi:10.1029/2003JB002942.

Weijermars, R., Jackson, M.P.A., and Vendeville, B., 1993. Rheological and tectonic modeling of salt provinces. *Tectonophysics*, 217, 143-174, doi.org/10.1016/0040-1951(93)90208-2.

Wong, T.F., David, C., and Zhu, W., 1997. The transition from brittle faulting to cataclastic flow in porous sandstones: Mechanical deformation. *Journal of Geophysical Research*, 102, B2, 3009-3025, doi.org/10.1029/96JB03281.

Zuluaga, L.F., Fossen, H., and Rotevatn, A., 2014. Progressive evolution of deformation band populations during Laramide fault-propagation folding: Navajo Sandstone, San Rafael monocline, Utah, USA. *Journal of Structural Geology*, 68, 66-81, doi.org/10.1016/j.jsg.2014.09.008.

VITA

William Ray Swanger II

Education

B.S. Geology (2016)
James Madison University, Harrisonburg, VA

Experience

Graduate Teaching / Research Assistant

UK Structure and Geodynamics Lab
Department of Earth and Environmental Sciences
University of Kentucky, 40506

Geologist

Virginia Department of Mines, Minerals, and Energy
Division of Geology and Mineral Resources
Charlottesville, VA, 22903

Contract Geologist

James Madison University
Department of Earth and Environmental Sciences
Harrisonburg, VA, 22807

Research Assistant

James Madison University
Department of Earth and Environmental Sciences
Harrisonburg, VA, 22807

Publications

Swanger, W.R., and Whitmeyer, S.J., 2021. Creating Geologic Maps in the 21st Century: A Case Study from Western Ireland. Springer field guidebook for structural geology and tectonics, vol. 1, 1-17, https://doi.org/10.1007/978-3-030-60143-0_1.

Swanger, W.R., Thigpen, J.R., Helfrich, A.L., and Spencer, B.M., 2020. Quantifying strain accommodation and deformation of wall rocks and overburden sequences proximal to salt diapirs in Salt Valley, Utah. Geological Society of America-Annual Meeting, Abstracts with Programs, Abstracts.

Occhi, M.E. and **Swanger, W.R.**, 2019. Geologic Map of the Beach Quadrangle, Virginia. Virginia Division of Geology and Mineral Resources Open-file Report 2018-03, 1:24,000-scale geologic map.

Whitmeyer, S.J., Pyle, E.J., Pavlis, T.L., **Swanger, W.R.**, and Roberts, L., 2019. Modern approaches to field data collection and mapping: Digital methods, crowdsourcing, and the future of statistical analyses. *Journal of Structural Geology*, doi.org/10.1016/j.jsg.2018.06.023

Haynes, J.T. and **Swanger, W.R.**, 2018. Geologic Map of Three Quarters of the Eagle Rock Quadrangle, Virginia. Virginia Division of Geology and Mineral Resources Open-file Report 2018-03, 1:24,000-scale geologic map.

Swanger, W.R., and Admassu, Y., 2018. Using Google Earth and Google Street View to Rate Rock Slope Hazards. *Environmental and Engineering Geoscience*, vol. 24, 237–250, doi: 10.2113/EEG-1922.

Heller, M.J., Biebuyck, A.J., and **Swanger, W.R.**, 2017. Geologic map of the Oriskany Quadrangle, Virginia. Virginia Division of Geology and Mineral Resources 2017 STATEMAP deliverable, 1:24,000-scale map.

Swanger, W.R., and Admassu, Y., 2016. Using Google Earth's street view to rate cut slopes along highways with respect to rockfall hazards. *Geological Society of America-Southeastern Section, Abstracts with Programs, Abstracts*.